



ELSEVIER

Journal of Structural Geology 26 (2004) 603–624

---

JOURNAL OF  
STRUCTURAL  
GEOLOGY

---

[www.elsevier.com/locate/jsg](http://www.elsevier.com/locate/jsg)

## Compaction localization in porous sandstones: spatial evolution of damage and acoustic emission activity

Patrick Baud<sup>a,\*</sup>, Emmanuelle Klein<sup>a</sup>, Teng-fong Wong<sup>b</sup>

<sup>a</sup>*Institut de Physique du Globe (CNRS/ULP), 5 rue Descartes, 67084 Strasbourg, France*

<sup>b</sup>*Department of Geosciences, State University of New York at Stony Brook, Stony Brook, NY 11794-2100, USA*

Received 13 March 2003; received in revised form 8 September 2003; accepted 11 September 2003

---

### Abstract

The coupled development of compaction and strain localization may significantly impact the stress field, strain partitioning and fluid transport. To investigate the phenomenon of compaction localization, mechanical deformation and microstructural observations were conducted on the Darley Dale, Rothbach, Berea, Bentheim and Diemelstadt sandstones with porosities ranging from 13 to 24%. The constitutive behavior, failure mode, acoustic emission (AE) activity and spatial distribution of damage were investigated. While our observations reveal a broad spectrum of geometric complexity associated with failure modes, two end-members can be distinguished: shear bands at relatively high angles and arrays of discrete compaction bands superparallel to the maximum compression direction, respectively. A hybrid localization mode involving high-angle shear bands and diffuse compaction bands was observed in sandstones with intermediate porosities. The discrete compaction bands in our laboratory samples are qualitatively similar to localization structures observed in the field. Whereas the development of high-angle shear bands is characterized by the continuous accumulation of AE, discrete bands are associated with episodic surges in AE that are characterized by an overall strain hardening trend punctuated by episodic stress drops.

© 2003 Elsevier Ltd. All rights reserved.

**Keywords:** Compaction bands; Sandstone; Acoustic emissions; Localization; Microstructure

---

### 1. Introduction

Strain localization occurs on all scales, from small laboratory samples up to crustal fault zones. Since localized deformation can significantly influence the stress field, strain partitioning and fluid transport, it is important to have a fundamental understanding of the mechanics of strain localization in rock. Shear and extensile discontinuities in the forms of faults and joints have been investigated quite thoroughly in the field and laboratory. These phenomena are accompanied by dilatancy, and accordingly attention has focused on strain localization that occurs in a dilatant rock. In contrast the development of localized failure in a compactant rock has not been studied systematically until recently.

Indeed there may be a misconception that a compactant rock does not fail in a localized mode. However, recent geologic (Mollema and Antonellini, 1996) and laboratory

(DiGiovanni et al., 2000; Olsson and Holcomb, 2000; Klein et al., 2001) studies have documented the occurrence of strain localization in compactant porous sandstones. The localized failure mode can be in the forms of conjugate shear or compaction bands oriented at relatively high angles (up to 90°) to the maximum compression ( $\sigma_1$ ) direction. Reassessment of bifurcation theory (Olsson, 1999; Issen and Rudnicki, 2000) and more extensive laboratory and microstructural investigations demonstrate the occurrence of such compaction localization phenomena in sandstones (with porosities ranging from 13 to 28%), generally associated with stress states in the transitional regime from brittle faulting to cataclastic flow (Wong et al., 2001).

Previous studies have focused on the mechanical behavior of porous sandstones in the two end-members of brittle faulting and cataclastic flow (Handin et al., 1963; Schock et al., 1973; Wong et al., 1997; Baud et al., 2000; Bésuelle et al., 2000). Under low effective pressure, damage is localized along a shear band, while the material undergoes dilatancy and strain softening (Menéndez et al., 1996; Mair et al., 2000; Wu et al., 2000; Bésuelle et al., 2003;

\* Corresponding author. Tel.: +33-3-902-40083; fax: +33-3-902-40125.  
E-mail address: pbaud@eost.u-strasbg.fr (P. Baud).

El Bied et al., 2002). At higher effective pressure, the material compacts and hardens with damage distributed homogeneously in the samples.

The spatial distribution of damage in both regimes was studied in detail at different stages of the deformation by Menéndez et al. (1996) and Wu et al. (2000) on Berea and Darley Dale sandstones, respectively. In the brittle regime, axial intragranular cracking and shear rupture of cemented grain contacts were observed in the rocks prior to failure. In the cataclastic flow regime, grain crushing and pore collapse were identified as the dominant mechanisms operative during cataclastic flow. In this study, we adopt a similar methodology to study four porous sandstones, focusing on several key questions on compaction localization.

While Wong et al. (2001) have documented that the stress states for the onset of compaction localization are associated with the transitional regime between brittle faulting and cataclastic flow, there have not been any systematic investigations of the spatial evolution of damage. How do the localized failure modes accommodate the progressive accumulation of deformation? The preliminary studies have documented two distinct modes of localization: once initiated a localized band may widen to develop a *diffuse* band of damage to accommodate the cumulative strain (Olsson, 1999), or alternatively further compaction is accommodated by the initiation of additional *discrete* bands that remain relatively narrow (Klein et al., 2001). What are the micromechanical processes associated with these localization modes and how are they related to the microstructure? How do the microstructure and geometric attributes of compaction bands in these laboratory-deformed samples compare with field observations? Acoustic emission (AE) measurements have proved to be an effective tool for characterizing the micromechanics. Damage processes involved with grain crushing and pore collapse are manifested by intense AE activity (Wong et al., 1997) while the development of localization is associated with spatial clustering of AE events (Olsson and Holcomb, 2000). Do the development of diffuse and discrete bands associated have distinct AE signatures?

To address these questions, we investigated the mechanical behavior, localized failure mode and deformation microstructure of five sandstones with porosities ranging from 13 to 24%. The samples were deformed at stress states at the brittle–ductile transition, and we characterized quantitatively the evolution of porosity, AE activity, as well as microcrack density and its anisotropy in the failed samples. The mechanical and microstructural data are compared with field observations and theoretical predictions.

## 2. Experimental methodology

Darley Dale, Rothbach, Berea, Bentheim and Diemelstadt sandstones (with nominal porosities of 13, 20, 21, 23

and 24%, respectively) are used in this study. The Darley Dale, Rothbach and Berea sandstones were from the same block studied by Wong et al. (1997), and the Bentheim sandstone was from the same block studied by Wong et al. (2001). The petrophysical properties are compiled in Table 1.

The samples were cored perpendicular to their sedimentary bedding and then ground to a cylindrical shape, with diameter of 18.4 mm and length of 38.1 mm. The Berea, Darley Dale, Diemelstadt and Rothbach sandstones samples were saturated with distilled water and deformed under fully drained conditions at a fixed pore pressure of 10 MPa. Adjustment of a pressure generator kept the pore pressure constant, and the pore volume change was recorded by monitoring the piston displacement of the pressure generator with a displacement transducer (DCDT). The porosity change was calculated from the ratio of the pore volume change to the initial bulk volume of the sample. For Bentheim sandstone, the nominally dry samples were dried in vacuum for a week at 80 °C. Longitudinal and transverse strains were measured by two electric resistance strain gauges (Baud et al., 2000). The volumetric strain was calculated from the strain gauge data by summing the axial strain and twice the transverse strain.

The sandstone samples were deformed at a nominal axial strain rate of  $1.3 \times 10^{-5} \text{ s}^{-1}$  in the conventional triaxial configuration at room temperature and under confining pressures ranging from 40 to 395 MPa (Wong et al., 1997; Baud et al., 2000). To record AE activity during triaxial experiments, we used a piezoelectric transducer mounted on the spacer attached to the jacketed sample. The AE signals were conditioned by a preamplifier (gain 40 dB, frequency response 1.5 kHz–5 MHz). To distinguish AE events from electric noise, a discriminator was used to check the amplitude and oscillational characteristics of the incoming signal. (See Zhang et al. (1990) for details.)

Samples at different stages of deformation were unloaded and retrieved from the pressure vessel. The deformed samples were first impregnated with epoxy and then sawed along a plane parallel to the axial direction to prepare petrographic thin-sections. Using optical microscopy the damage states in the thin-sections were characterized. As described later some of the samples failed locally along diffuse bands, with intense damage at the center of a band that decreased laterally. To identify such a diffuse band it is necessary to resolve in fine detail the spatial distribution of crack density. For each of these samples an area of  $16.3 \times 35.4 \text{ mm}^2$  centrally located in the thin section was divided into  $10 \times 29$  subregions, each of which had an area of  $1.63 \times 1.22 \text{ mm}^2$ . A stereological technique (Wu et al., 2000) was used to measure the crack densities (in the two orthogonal directions parallel and perpendicular to  $\sigma_1$ ). In each subregion a test array made up of five lines (spaced 0.24 mm apart) in the axial direction and another five lines in the orthogonal direction (spaced 0.33 mm apart) was used. Reflected images were acquired at a magnification of

Table 1

Petrophysical description of the five sandstones investigated in this study

Sandstone name	Porosity (%)	Grain radius (mm)	Composition
Darley Dale	13	0.17	Quartz: 66%, feldspar: 21%, mica: 3%, clay: ~6%
Rothbach	19.9	0.23	Quartz: 68%, feldspar: 16%, oxides and mica: 3%, clay: ~6%
Berea	21	0.13	Quartz: 71%, feldspar: 10%, carbonate: 5%, clay: ~10%
Bentheim	22.8	0.105	Quartz: 95%, kaolinite: 3%, orthoclase: 3%
Diemelstadt	24.3	0.08	Quartz: 68%, feldspar: 26%, oxides: 4%, micas: 2%

100 × , and we counted the number of crack intersections with the test array.

We denote the linear intercept density (number of crack intersections per unit length) for the array oriented parallel to  $\sigma_1$  by  $P_L^\parallel$ , and that for the perpendicular array by  $P_L^\perp$ . For each of the 290 subregions these two stereological parameters ( $P_L^\parallel$  and  $P_L^\perp$ ) provide a quantitative measure of the crack density and anisotropy. Since the spatial distribution of damage is approximately axisymmetric in a triaxially compressed sample, the crack surface area per unit volume ( $S_v$ ) is given by:

$$S_v = \frac{\pi}{2} P_L^\perp + \left(2 - \frac{\pi}{2}\right) P_L^\parallel \quad (1)$$

and the anisotropy of crack distribution can be characterized by the stereological parameter:

$$\Omega_{23} = \frac{P_L^\perp - P_L^\parallel}{P_L^\perp + (4/\pi - 1)P_L^\parallel} \quad (2)$$

that represents the ratio between the surface area of cracks parallel to  $\sigma_1$  and the total crack surface area (Underwood, 1970; Wong, 1985).

### 3. Mechanical data

In this paper we will use the convention with the compressive stresses and compactive strains taken as positive. We will denote the maximum and minimum (compressive) principal stresses by  $\sigma_1$  and  $\sigma_3$ , respectively. The pore pressure will be denoted by  $P_p$ , and the difference  $P_c - P_p$  between the confining pressure ( $P_c = \sigma_2 = \sigma_3$ ) and pore pressure will be referred to as the ‘effective pressure’  $P_{\text{eff}}$ . The effective mean stress ( $(\sigma_1 + 2\sigma_3)/3 - P_p$ ) will be denoted by  $P$  and the differential stress  $\sigma_1 - \sigma_3$  by  $Q$ .

We performed a series of experiments through the brittle–ductile transition. The conditions were chosen such that dilatancy was absent in all these experiments. To underscore the compactive failure behavior, we plot in Fig. 1a–d the effective mean stress as a function of porosity change. The nonhydrostatic and hydrostatic loadings are coupled in a conventional triaxial compression experiment. If the axial stress increases by an increment  $\Delta\sigma_1$  while the confining and pore pressures are maintained constant, then the effective mean stress  $P$  and differential stress  $Q$  would increase by the amounts  $\Delta\sigma_1/3$  and  $\Delta\sigma_1$ , respectively. If

porosity change is elastic then it is solely controlled by the hydrostatic stresses and independent of the differential stress, and therefore the triaxial data (solid curves) in Fig. 1 should coincide with the hydrostat (dashed curves).

Any deviation from the hydrostat would imply that the porosity change in a triaxial compression experiment depends on not only the effective mean stress, but also the deviatoric stresses. This in turn implies the onset of inelastic yield. In all the experiments shown in Fig. 1 the triaxial curve for a given effective pressure coincided with the hydrostat up to a critical stress state (indicated by  $C^*$ ), beyond which there was an accelerated decrease in porosity in comparison with the hydrostat. At stress levels beyond  $C^*$  the deviatoric stress field provided a significant contribution to the compactive strain, and this phenomenon of inelastic yield by ‘shear-enhanced compaction’ (Wong et al., 1997) is attributed to the inception of grain crushing and pore collapse in the sandstone (Menéndez et al., 1996). Table 2 compiles data of the compactive yield stress  $C^*$  for the samples used in this study.

Figs. 2–5 show the differential stress  $Q$  ( $= \sigma_1 - \sigma_3$ ) and AE activity as a function of axial strain for selected experiments. Two features of the stress–strain curves should be noted. First, there is an overall trend for the post-yield slope to increase with increasing pressure, a manifestation of the transition from strain softening to hardening. Second the overall hardening (or softening) trend is punctuated by episodic stress drops in some of the sandstones. In the Bentheim sandstone (Fig. 2) this behavior was observed over a wide range of pressures (90–395 MPa), independent of whether the overall trend was strain hardening or softening. In Berea sandstone, episodic stress drops with relatively small amplitudes were observed at an effective pressure of 200 MPa, while single stress drops were observed at effective pressures of 75 and 150 MPa (Fig. 3). Qualitatively similar behavior was observed in the Rothbach sandstone (Fig. 4). In contrast we did not observe any episodic stress drops in the relatively compact Darley Dale (Fig. 5).

The AE data in these experiments follow two common trends that have been reported in earlier studies (Wong et al., 1997; Baud et al., 2000; Wu et al., 2000; Klein et al., 2001; Bésuelle et al., 2003). First, a significant increase in AE activity is associated with the onset of shear-enhanced compaction at the critical stress  $C^*$ . Second there is an overall trend for the cumulative AE count to increase with

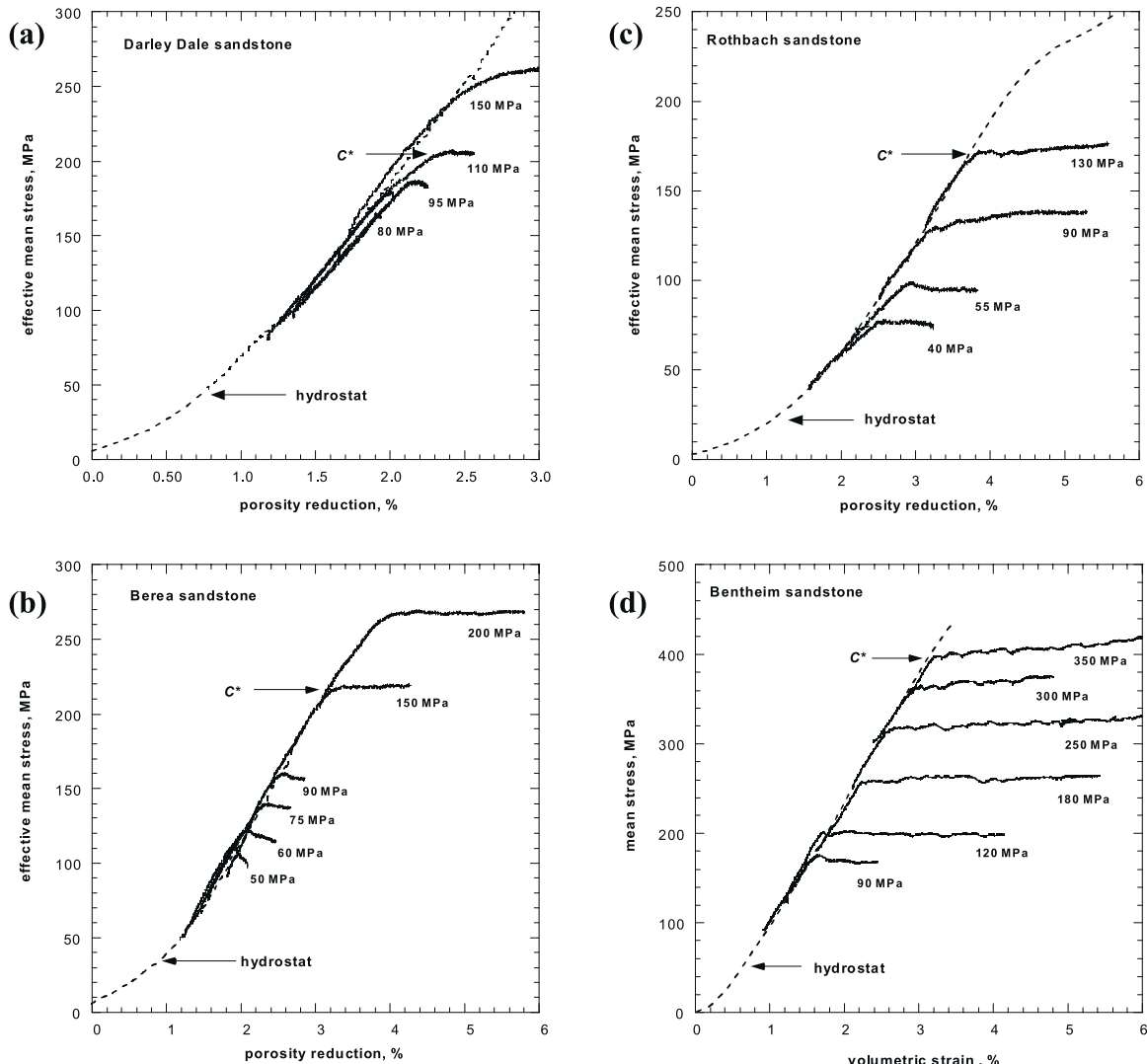


Fig. 1. (a) Effective mean stress versus porosity reduction of Darley Dale sandstone. For reference, the hydrostat is shown as a dashed curve. (b) Effective mean stress versus porosity reduction of Berea sandstone. (c) Effective mean stress versus porosity reduction of Rothbach sandstone. (d) Mean stress as a function of volumetric strain of nominally dry Bentheim sandstone.

strain, a manifestation of the progressive increase of damage.

However there is also an important attribute of the AE activity (not evident in the cumulative count presented in earlier studies), which we will highlight here by differentiating the cumulative count to obtain the AE rate. Two distinct types of activity can be identified on the basis of the AE rate.

- In experiments on the Bentheim, Rothbach and Berea sandstones that showed episodic stress drops, each of the stress drops was associated with an appreciable surge in AE rate (Figs. 2–4). A larger stress drop is associated with a more significant surge in AE rate. Such activity associated with multiple pulses of AE events and peaks in the AE rate will be referred to as ‘*p*-type’. As discussed below our microstructural observations

showed that *p*-type AE activity is associated with the spatial clustering of damage in zones aligned perpendicular to  $\sigma_1$ .

- In samples that underwent compactive failure without any stress drops (Figs. 3–5) a monotonic decrease of AE rate was usually observed after an initial surge at the critical stress  $C^*$ . Such AE activity will be referred to as the ‘*m*-type’. Similar AE activity has also been observed in experiments under high confinement when compactive failure occurred without any development of strain localization. Our microstructural observations showed that *m*-type AE activity in samples that failed by compaction localization is associated with the development of diffuse damage zones at relatively high angles to  $\sigma_1$ .

Preliminary experiments were also conducted to investigate the development of compaction localization in the

Table 2  
Mechanical data of the samples investigated in this study

Effective pressure (MPa)	Compactive yield stress ( $C^*$ )		Maximum axial strain (%)	Acoustic emission activity	Comments on failure modes
	Differential stress: $Q = \sigma_1 - \sigma_3$ (MPa)	Effective mean stress: $P = (\sigma_1 + 2\sigma_3)/3 - P_p$ (MPa)			
Darley Dale sandstone					
80	251	164	3	<i>m</i> -type	Conjugate high-angle shear bands
90	264	178	2.66	<i>m</i> -type	Conjugate high-angle shear bands
95	269	186	3.75	<i>m</i> -type	Conjugate high-angle shear bands
110	270	200	3.96	<i>m</i> -type	Cataclastic flow
Berea sandstone					
50	182	111	2.5	<i>m</i> -type	Conjugate high-angle shear bands
60	179	120	2.66	<i>m</i> -type	Conjugate high-angle shear bands
75	184	137	2.4	<i>m</i> -type	Conjugate high-angle shear bands
90	190	154	2.4	<i>m</i> -type	Conjugate high-angle shear bands
150	191	214	3.2	<i>p</i> -type	Diffuse compaction bands
200	178	260	3.6	<i>p</i> -type	Discrete and diffuse compaction bands
Rothbach sandstone					
40	112	77	2.6	<i>m</i> -type	Conjugate high-angle shear bands
55	117	95	3	<i>m</i> -type	Conjugate high-angle shear bands
90	122	130	4.4	<i>m</i> -type	Conjugate high-angle shear bands
130	125	172	3.6	<i>p</i> -type	Diffuse compaction bands
Bentheim sandstone					
90	239	170	2.9	<i>p</i> -type	Discrete compaction bands + high-angle shear bands
120	245	202	3.8	<i>p</i> -type	Discrete compaction bands
150	240	230	2.2 <sup>a</sup>	<i>p</i> -type	Discrete compaction bands
180	230	257	4.4	<i>p</i> -type	Discrete compaction bands
250	191	314	7 <sup>a</sup>	<i>p</i> -type	Discrete compaction bands
300	170	357	3.1	<i>p</i> -type	Discrete compaction bands
350	136	396	9.5 <sup>a</sup>	<i>p</i> -type	Discrete compaction bands
395	90	425	3	<i>p</i> -type	Discrete compaction bands
Diemelstadt sandstone					
80	79	107	3.5	<i>m</i> -type	Diffuse compaction bands
160	28	170	4	<i>p</i> -type	Discrete compaction bands

<sup>a</sup> The microstructure of this sample was not studied.

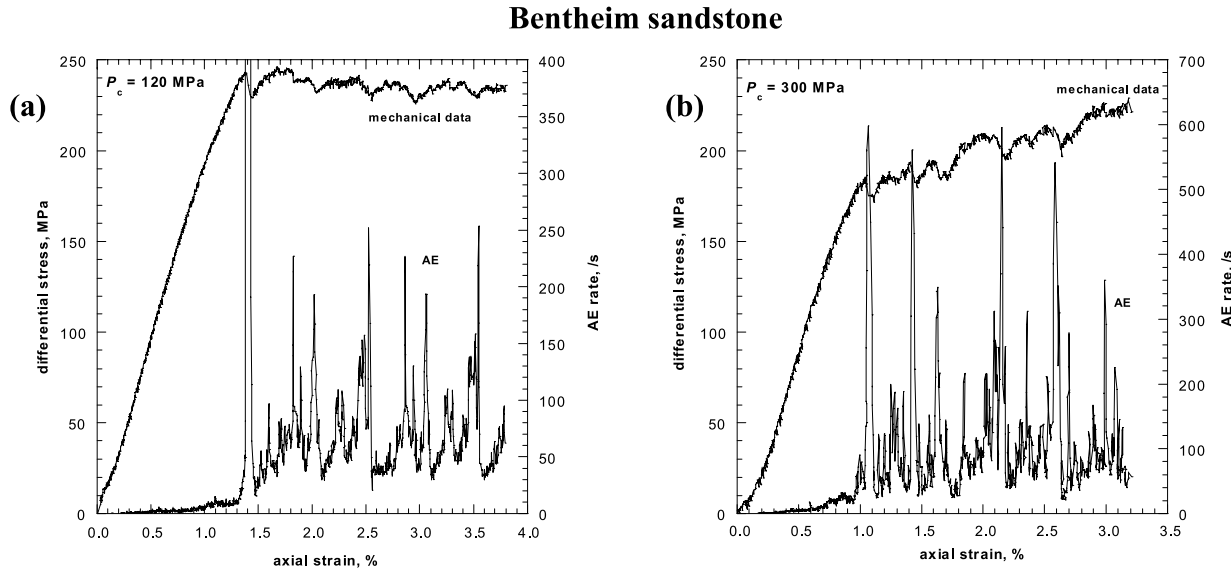


Fig. 2. Principal stress difference and rate of acoustic emissions as AE per second versus axial strain for triaxially deformed dry samples of Bentheim sandstone at 120 MPa (a) and 300 MPa (b) of confining pressure. Principal stress  $\sigma_1$  was along the axial direction.

Diemelstadt sandstone at effective pressures of 80 and 160 MPa. The mechanical data and AE activity are shown in Fig. 6.

#### 4. Microscopic observations and quantitative evaluation of damage

The preliminary data of Wong et al. (2001) demonstrate that compaction localization develops in stress states associated with the brittle–ductile transition. Mechanical data (Wong et al., 1997; Klein et al., 2001) as well as microstructural observations of the brittle and ductile end-members (Menéndez et al., 1996; Wu et al., 2000; Wong et al., 2001; Bésuelle et al., 2003) have guided us in identifying the pressure ranges that correspond to the transitional regime of interest (Table 2).

For each pressure condition a sample was deformed to beyond the onset of shear-enhanced compaction, and the microstructure in the deformed sample was then investigated. The maximum axial strain attained in each sample is compiled in Table 2. It is of importance to investigate not only the onset but also the development of compaction localization, which would require detailed microstructural observations on a suite of several samples compacted to different stages at the same pressure condition. While it is beyond the scope of the present study to undertake such an involved endeavor for all five sandstones, we have focused on the initial development of compaction localization, with the exception of the Bentheim sandstone for which the development of localization as a function of strain was also investigated. Experimental conditions under which the samples were deformed are compiled in Table 2, with comments on the type of AE activity and failure mode.

Damage evolution is quantified by the spatial distribution

of microcrack density. The development of an elongate, connected cluster of anomalous damage (manifested by high crack density) that extends over several grains is considered as a proxy for compaction localization. Since our observations have revealed a broad spectrum of geometric attributes associated with compaction localization, it is important to first define several terms adopted in later discussion.

- A localized structure that is subperpendicular to the maximum principal stress  $\sigma_1$  will be referred to as a ‘compaction band’ (Olsson, 1999; Issen and Rudnicki, 2000). A localized structure that subtends a relatively high angle (say 45–80°) to  $\sigma_1$  will be referred to as a ‘high-angle shear band’. It should be noted that the latter is akin to a ‘compactive shear band’ as described by Bésuelle (2001).
- A localized tabular structure of only a few (say  $\leq 3$ ) grains thick will be referred to as a ‘discrete band’. A structure with a thickness of many more grains will be referred to as a ‘diffuse band’. High-angle shear bands commonly develop as conjugate sets of diffuse bands. A compaction band may be discrete or diffuse. Discrete compaction bands commonly develop as a subparallel array, with the cumulative strain accommodated by the initiation of additional discrete bands. In contrast, a diffuse compaction band accommodates the cumulative strain by the lateral propagation of damage.

#### 5. Two end-members of compaction localization

Our microstructural observations have revealed a broad spectrum of geometric complexity associated with

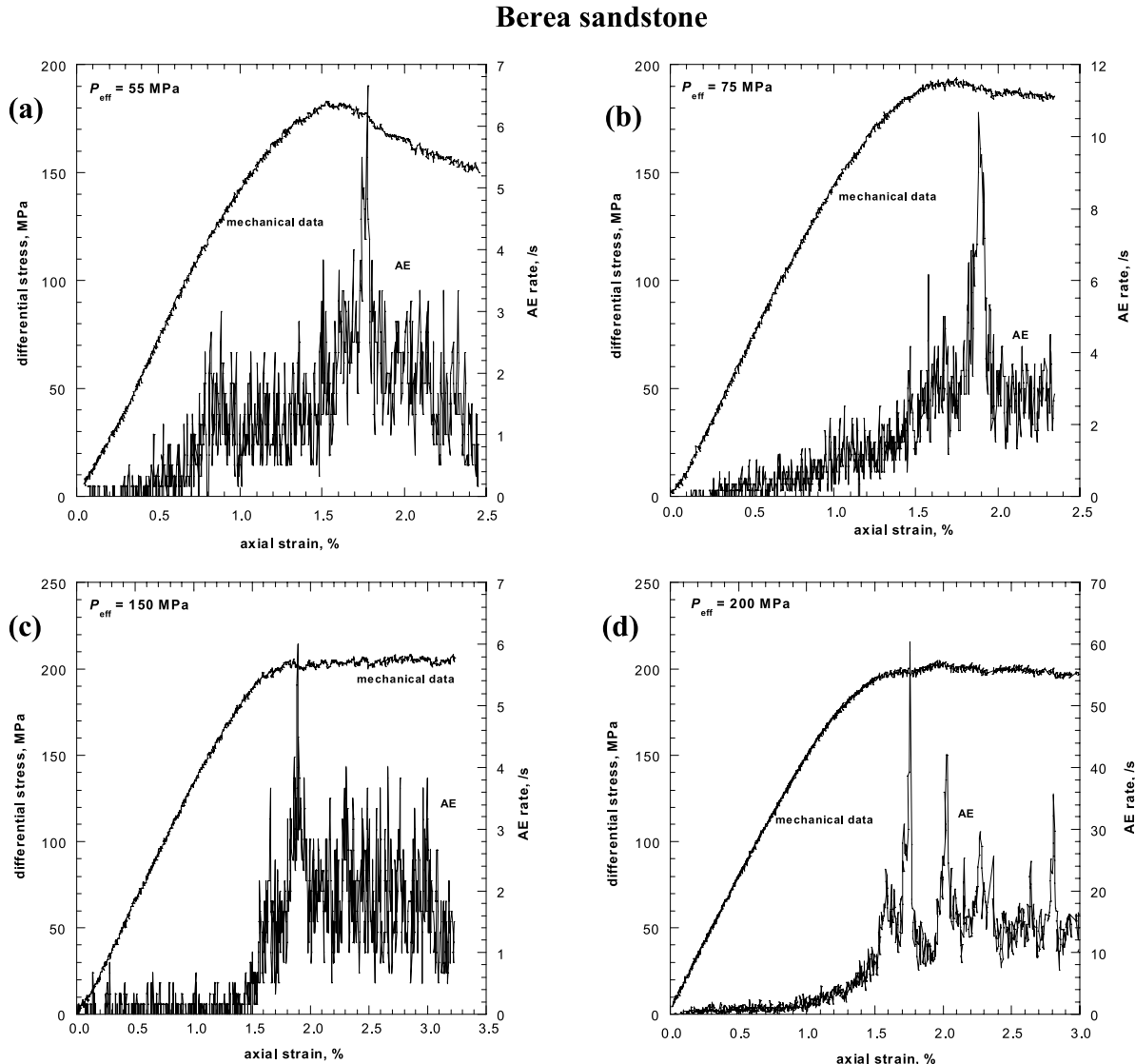


Fig. 3. Principal stress difference and rate of acoustic emissions per second versus axial strain for triaxially deformed samples of Berea sandstone at 55 MPa (a), 75 MPa (b), 150 MPa (c), and 200 MPa (d) effective pressure.

compaction localization, with two end-members represented by the Bentheim and Darley Dale sandstones. As one of the end-members the Bentheim sandstone is distinguished by three localization characteristics. First, compaction localization was observed over the widest range of pressure (90–395 MPa). Second, the stress–strain curve is punctuated by episodic stress drops, accompanied by *p*-type AE activity. Third, subparallel arrays of discrete compaction bands were commonly observed (Table 2). This localization mode was documented by Wong et al. (2001), who presented micrographs of four Bentheim sandstone samples (deformed at confining pressures of 90, 120, 180 and 300 MPa) to just beyond  $C^*$ . Fig. 7a shows the microstructure of such a sample deformed to an axial strain of 4% at 180 MPa confining pressure.

Here we also present additional microstructure that illustrates the evolution of localization with strain. Fig. 8

presents the micrographs of four samples deformed at 300 MPa confining pressure to axial strains of 1.4–6.0%. The onset of shear-enhanced compaction was manifested by discrete compaction bands that initiated in short segments near either end of the sample (Fig. 8a). With increasing strain the discrete bands cut through the cross-section of the sample, and as the cumulative number of bands increased, they clustered to constitute two subparallel arrays that spread towards the center of the sample (Fig. 8b and c). At 6% axial strain the discrete compaction bands were pervasive in the sample (Fig. 8d). Mechanical tests to higher strain showed that episodic stress drops and AE surges were inhibited beyond ~6% axial strain. That the numbers of discrete bands, stress drop events and AE peaks are correlated implies that an individual stress drop event arises from the unstable propagation of a discrete compaction band

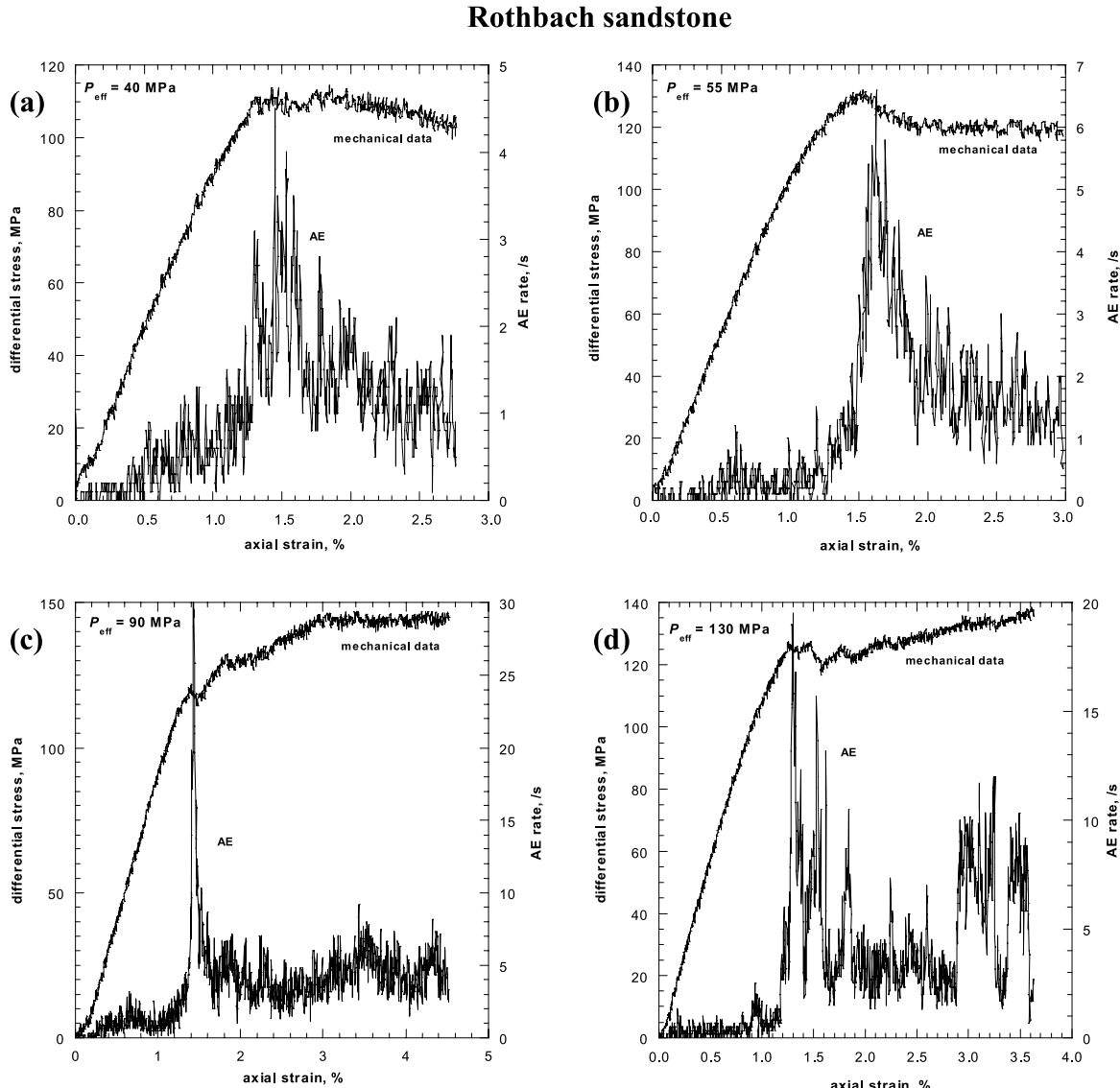


Fig. 4. Principal stress difference and rate of acoustic emissions per second versus axial strain for triaxially deformed samples of Rothbach sandstone at 40 MPa (a), 55 MPa (b), 90 MPa (c), and 130 MPa (d) effective pressure.

normal to  $\sigma_1$ , with intensive grain-scale cracking that induces a concomitant surge of AE activity.

Although a discrete compaction band has an overall direction subperpendicular to  $\sigma_1$ , it appears tortuous on the grain scale under the microscope. A few of them intersect each other, rendering it difficult to unambiguously determine the number of such discrete bands in the highly strained samples. The detailed view in Fig. 9 shows that typically the average width of a discrete compaction band is  $\sim 0.5 \text{ mm}$ , comparable with the grain size. Inside the band, the grains had been crushed to form very small fragments, so the bands can be identified by relatively dark areas of intense comminution visible by eye in a thin section. In the Bentheim sandstone the damage in the discrete bands is so intense that it is very difficult to determine quantitatively the crack densities except at very high magnification. Outside the bands, few cracks were observed and the

damage was negligible beyond a lateral distance of about two or three grains.

Our preliminary study of Diemelstadt sandstone indicates that its localization mode is similar to that of Bentheim sandstone. Fig. 7b shows the development of discrete compaction bands in a saturated sample of the Diemelstadt sandstone deformed to an axial strain of 3.9% at effective pressure of 160 MPa. The shear-enhanced compaction was accompanied by small stress drops and *p*-type AE activity (Fig. 6).

The other end-member of compaction localization is represented by the Darley Dale sandstone with three distinct characteristics. First, localization was observed over the narrowest range of effective pressure (80–95 MPa). Second, the AE activity is of the *m*-type (Fig. 5). Third, high-angle shear bands were observed in all our failed samples (Table 2). This localization mode was documented

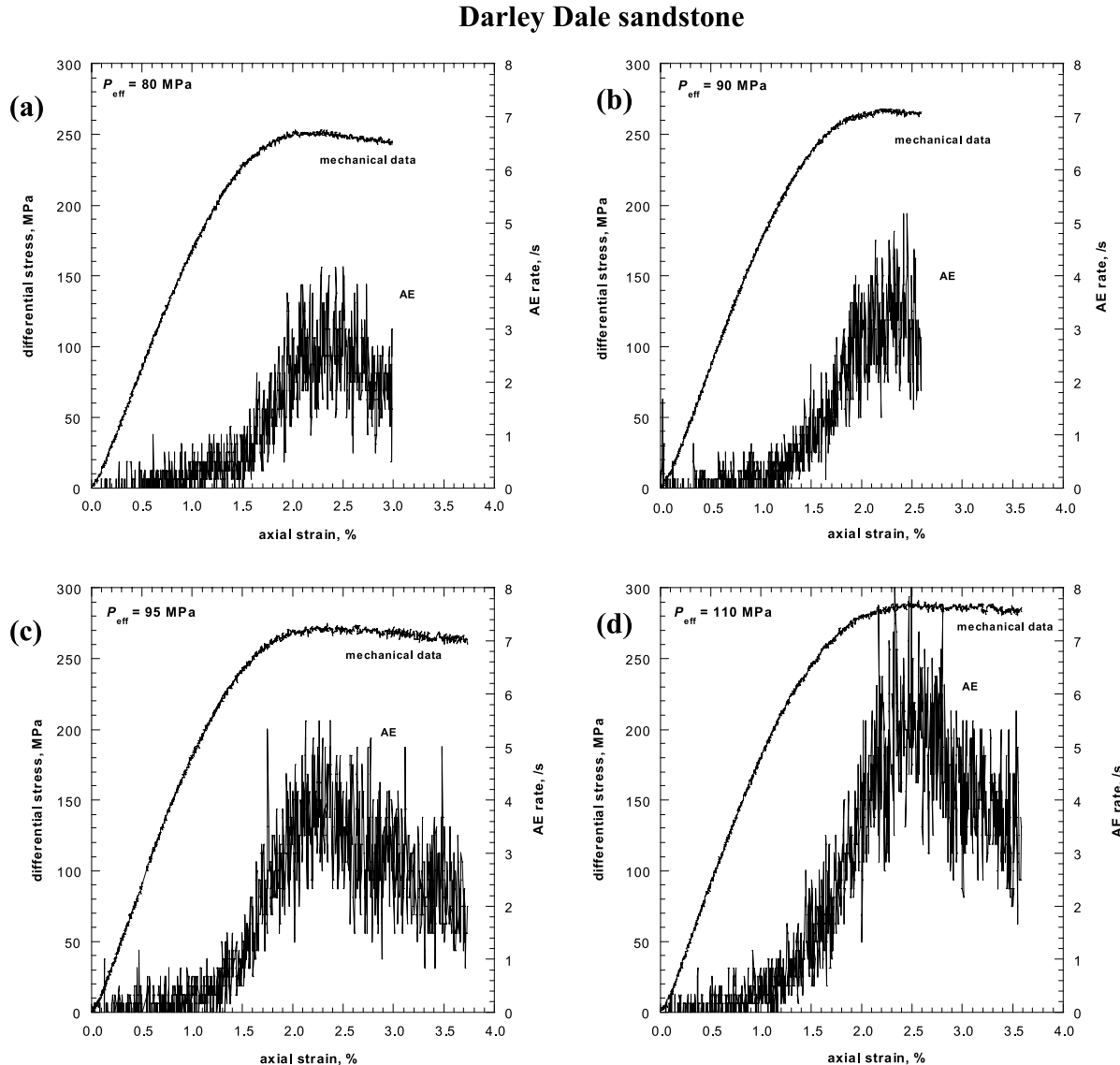


Fig. 5. Principal stress difference and rate of acoustic emissions per second versus axial strain for triaxially deformed samples of Darley Dale sandstone at 80 MPa (a), 90 MPa (b), 95 MPa (c), and 110 MPa (d) effective pressure.

by Wong et al. (2001), who presented micrographs of two samples (deformed at effective pressures of 90 and 95 MPa) to just beyond  $C^*$  and contrasted them with two other samples with brittle faulting at effective pressure of 80 MPa and delocalized cataclastic flow at 110 MPa, respectively. Fig. 10a shows the spatial distribution of damage in a sample deformed at 95 MPa effective pressure. The highest crack densities were found at the upper end of the sample, where conjugate high-angle shear bands had developed. Inside the conjugate shear bands, we observed intense grain crushing (Fig. 10b) as well as axial cracking (Fig. 10c). Outside the band some axial cracks and evidence of grain crushing in isolated areas were observed (Fig. 10d), but overall the damage was significantly less intense than that in the shear bands.

In Berea sandstone, the localization behavior is a hybrid of these two end-members. The spatial distribution of

damage in Berea sandstone at the brittle–ductile transition is summarized in Fig. 11. In an unstressed sample of Berea sandstone, Menéndez et al. (1996) found an average value of  $S_v$  of  $\sim 3 \text{ mm}^{-1}$  for the specific microcrack surface area. To underscore the spatial heterogeneity we set the lower limit at this value for the color scale in this figure. At effective pressures up to 150 MPa, damage was localized at either end of a sample and did not spread toward the center, even in samples deformed to a maximum axial strain of 3.2%. In a localized cluster the damage level was relatively high, with  $S_v$  about four to five times the nominal value in the rest of the sample. Fig. 12a presents details of a sample deformed at 90 MPa of effective pressure. At one end of the sample, high-angle conjugate shears developed as diffuse bands that emanated from both corners. The AE activity and stress–strain curve of this experiment were qualitatively similar to those shown in Fig. 3b, and our interpretation is

### Diemelstadt sandstone

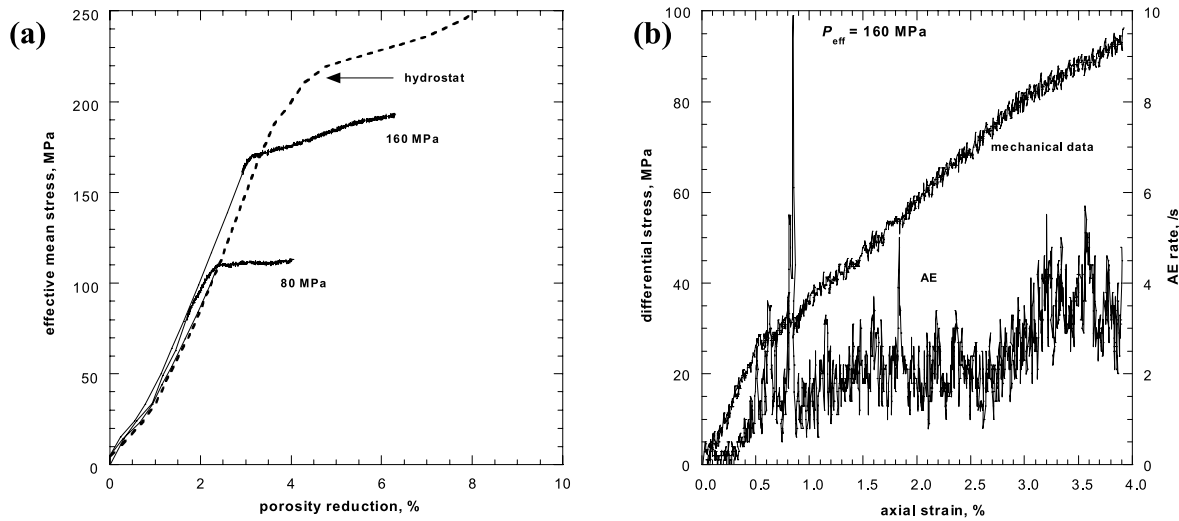


Fig. 6. (a) Effective mean stress versus porosity reduction of Diemelstadt sandstone. For reference, the hydrostat is shown as a dashed curve. (b) Principal stress difference and rate of acoustic emissions per second versus axial strain for a triaxially deformed sample of Diemelstadt sandstone at 160 MPa effective pressure.

that the high-angle shear bands had nucleated in the vicinity of the peak stress. With the accumulation of strain the high-angle shear bands widened laterally and evolved to become diffuse bands, manifested by a progressive increase of AE events as *m*-type activity. The detailed view shows that intense grain crushing had occurred in the core of compactive shear band (Fig. 12b), with appreciable

intragranular cracking in the periphery with a lateral dimension spanning over 6–8 grains (Fig. 12c).

A different localization mode was involved at higher effective pressures (Table 2). At 150 MPa effective pressure, diffuse compaction bands were observed (Fig. 11e). In this sample the damage remained confined to about 30% of the thin section. Fig. 13a illustrates the geometric complexity of the microstructure in a sample deformed at effective pressure of 200 MPa: compaction bands were observed not only at both ends, but also in the central part of the thin section. Altogether the highly damaged area (with  $S_v \sim 4$  times the nominal value) covers  $\sim 50\%$  of the area of the thin section. The compaction bands near both ends are diffuse, but the ones near the center are relatively narrow. One of these discrete bands is shown in detail in Fig. 13b. The width of this band is about two grains and it has a certain tortuosity at the grain scale. The grains inside the discrete band had been crushed intensely, but beyond a distance of about two grains there was almost no microcracking (Fig. 13c).

The AE activity is of the *p*-type in this pressure range (Fig. 3d). Our interpretation of the damage evolution is that the compaction bands in the Berea sandstone had initiated as discrete bands associated with the AE peaks. Although the AE signature is qualitatively similar to that in the Bentheim sandstone, the propagation of a discrete band in the Berea sandstone seems to have been more stable. Whereas a discrete compaction band in the Bentheim sandstone readily propagates unimpeded to cut through the cross-section, its counterpart in the Berea sandstone would be arrested at some point inside the sample. The cumulative deformation was accommodated by the development of such relatively short discrete bands, which would interact and coalesce to

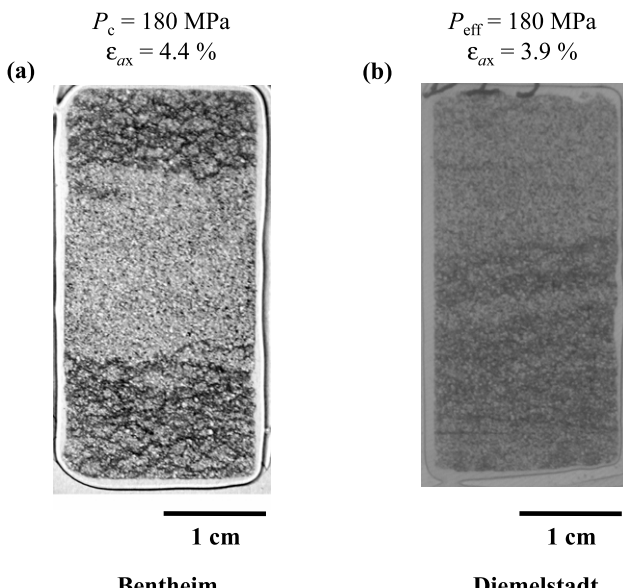


Fig. 7. Transmission optical micrographs of (a) Bentheim sandstone sample deformed at 180 MPa confining pressure to maximum axial strain of 4.4%, and (b) Diemelstadt sandstone sample deformed at 160 MPa effective pressure to maximum axial strain of 3.9%. The dark bands are associated with significant comminution. The width of each thin section is  $\sim 18$  mm. Principal stress  $\sigma_1$  was along the axial direction.

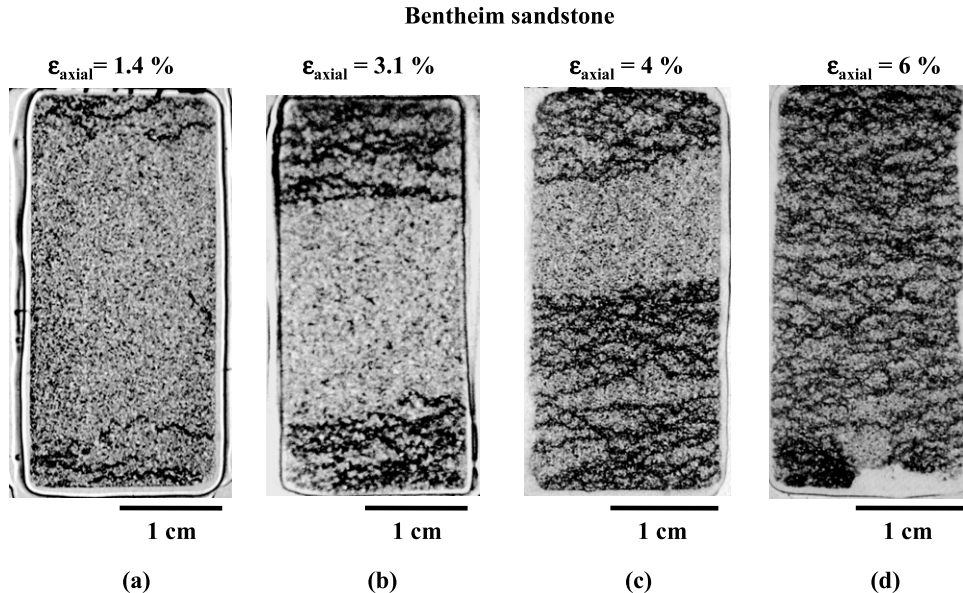


Fig. 8. Transmission optical micrographs of Bentheim sandstone samples deformed at 300 MPa confining pressure after different levels of axial strain: 1.4% (a), 3.1% (b), 4% (c), and 6% (d). The dark bands are associated with significant comminution. The width of each thin section is  $\sim 18$  mm. Principal stress  $\sigma_1$  was along the axial direction.

form the complex and diffuse structures. At effective pressures beyond 250 MPa, the AE activity is of the *m*-type and damage distribution in a failure sample is delocalized (Menéndez et al., 1996).

The hybrid localization behavior we observed in Berea sandstone is qualitatively similar to that in Rothbach sandstone. Preliminary microstructural observations on the latter have been presented by Bésuelle et al. (2003). In Fig. 14 we show a series of micrographs to illustrate the localization modes. Between 40 and 90 MPa (Fig. 14a–c), the compaction localization was predominately by conjugate shear

bands, whereas diffuse compaction bands were observed at 130 MPa of effective pressure (Fig. 14d).

## 6. Discussion

### 6.1. Compaction localization and failure mode in the brittle–ductile transition: the influence of stress and porosity

Wong et al. (2001) concluded that localized failure modes involving compaction bands and high-angle shear

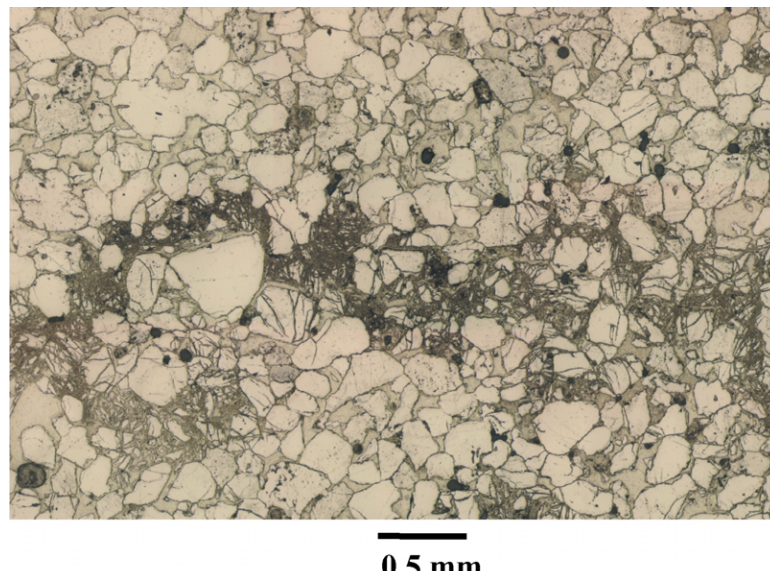


Fig. 9. Mosaic of micrograph showing the details of a discrete compaction band. The width of the band is about two grains. Principal stress  $\sigma_1$  was along the axial direction.

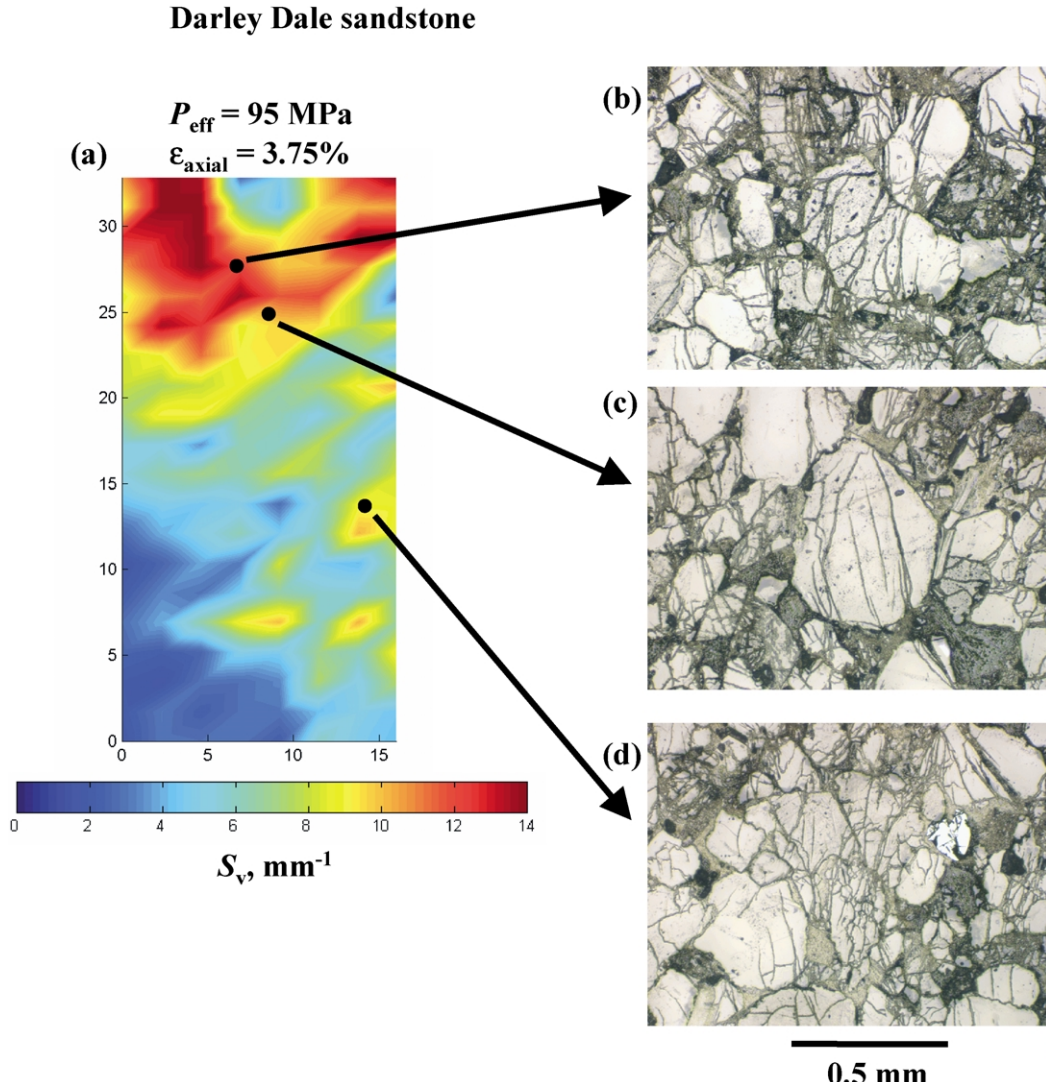


Fig. 10. (a) Spatial distribution of specific surface area in a sample of Darley Dale sandstone deformed at  $P_{\text{eff}} = 95 \text{ MPa}$ . (b) Extensive grain crushing in a compaction zone. (c) Area where axial cracking dominate. (d) Area outside the compaction zone where damage was important. The  $\sigma_1$  direction is vertical.

bands could develop in sandstones (with porosities ranging from 13 to 28%) while undergoing shear-enhanced compaction. They also observed that the phenomenon of compaction localization is associated with stress states in the transitional regime from brittle faulting to cataclastic flow. While these conclusions are corroborated in the present study, we have also elucidated the influence of pressure and porosity on the localization modes.

In Fig. 15 we summarize in the stress space the influence of effective pressure on the brittle–ductile transition and localization mode in four sandstones. We do not provide a summary on the Diemelstadt sandstone due to the preliminary nature of our data at this stage (Fortin et al., 2003). The open symbols correspond to the peak stress for samples that fail by brittle faulting. The dark symbols correspond to the compactive yield stress  $C^*$  for the onset of shear-enhanced compaction. Damage maps that indicate the localization mode are also shown for selected stress states.

In addition to data acquired in this study, we have included the mechanical and microstructural data of Wong et al. (1997), Baud et al. (2000), Wu et al. (2000), Klein et al. (2001), Wong et al. (2001) and Bésuelle et al. (2002).

The brittle–ductile transition and localization modes in the Darley Dale sandstone represent one of the end members (Fig. 15a). In an experiment at 10 MPa effective pressure the sample failed by development of a shear band at  $\sim 30^\circ$  to  $\sigma_1$ , which is characteristic of the brittle faulting regime. At effective pressures  $\geq 110 \text{ MPa}$  the samples failed by distributed cataclastic flow without any indication of strain localization. In the transitional regime compaction localization developed in the form of a high-angle shear band ( $\sim 45^\circ$  to  $\sigma_1$ ) at effective pressure of 80 MPa and conjugate shear bands at effective pressures of 90 and 95 MPa. Compaction localization occurs in a very narrow range of effective pressures and it involves a single mode, namely, the development of high-angle shear bands.

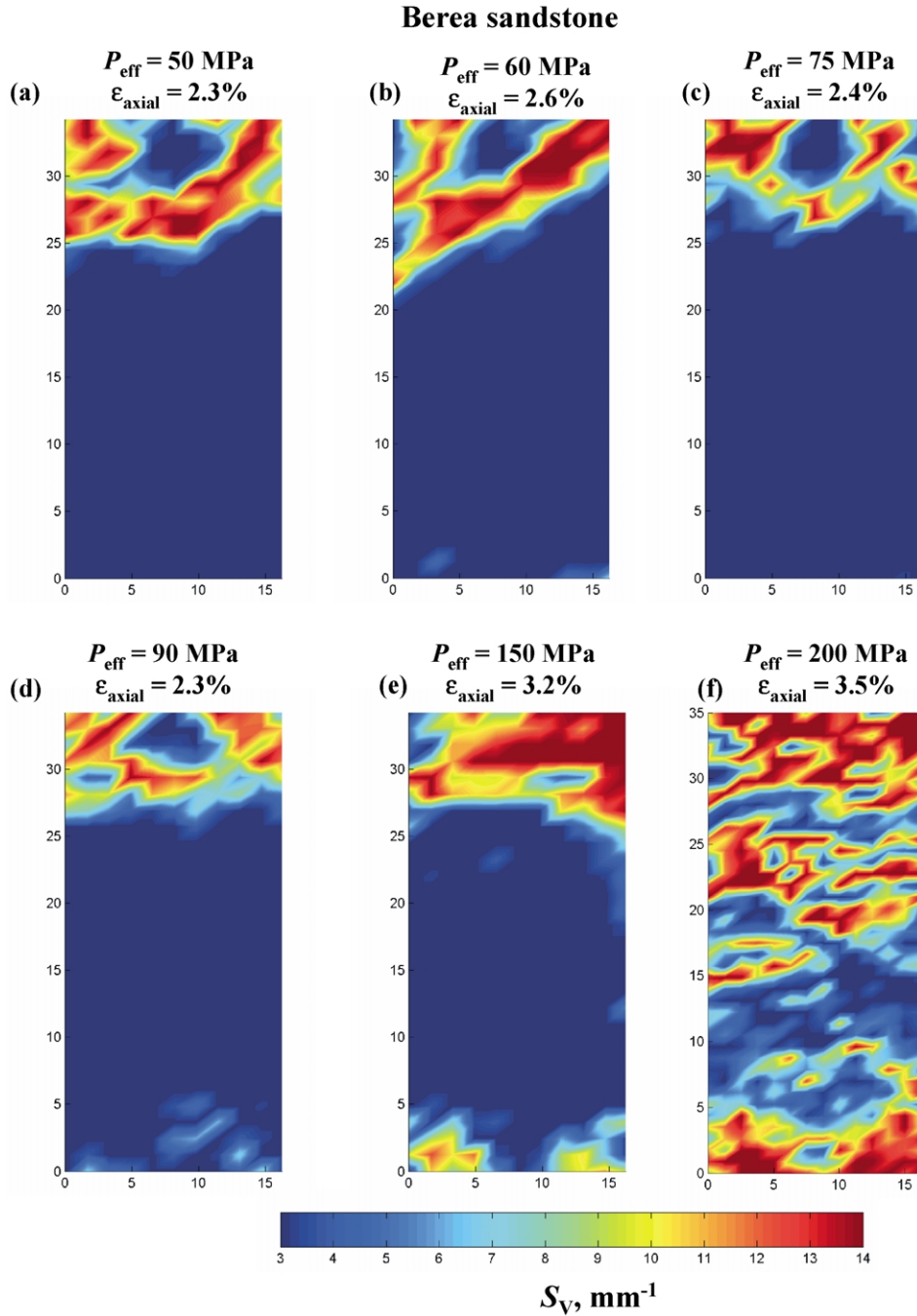


Fig. 11. Spatial distribution of specific surface area in samples of Berea sandstone deformed in the brittle–ductile transition at 50 MPa (a), 60 MPa (b), 75 MPa (c), 90 MPa (d), 150 MPa (e), and 200 MPa (f) effective pressure. The  $\sigma_1$  direction is vertical.

Bentheim sandstone represents the other end member. Compaction localization occurred over a very wide pressure range (90–395 MPa) and it involved a single mode, namely, the formation of discrete compaction bands in a subparallel array (Fig. 15d). Our preliminary data show that the Diemelstadt sandstone (Fig. 7b) also belongs to this end-member. A conceptual model of how this end member evolves to accommodate the cumulative strain is shown in Fig. 16a.

Intermediate between these two end members is the

compaction localization behavior in Berea and Rothbach sandstones, which involved a hybrid of two failure modes. In the Berea sandstone high-angle shear bands were observed at an effective pressures of 50 and 75 MPa, and the failure mode switched to diffuse compaction bands at 150 and 200 MPa (Fig. 15b). Similarly in the Rothbach sandstone high-angle shear bands were observed at an effective pressure of 55 MPa, and the failure mode switched to diffuse compaction bands at 130 MPa (Fig. 15c).

The end-member scenario documented here for the

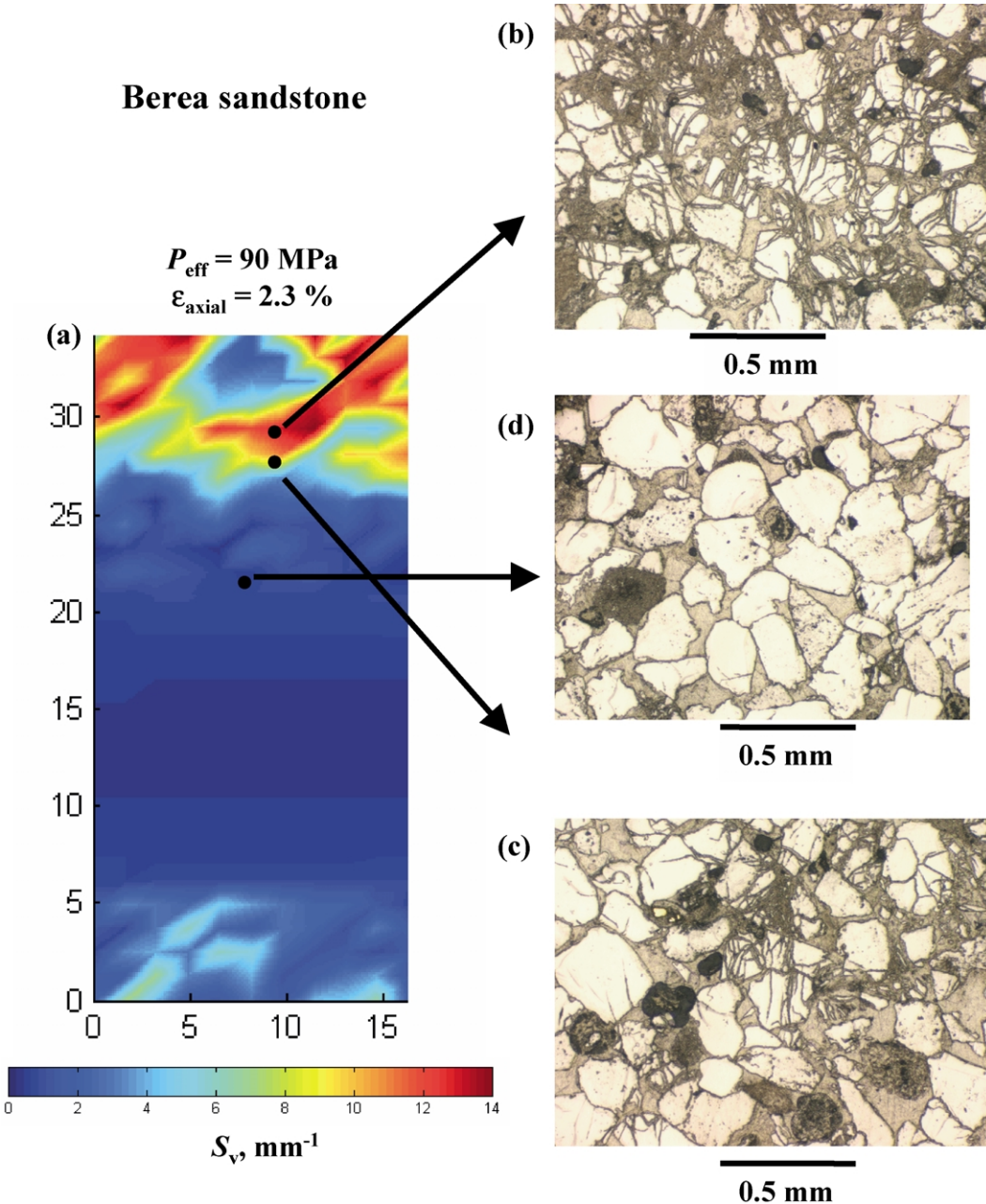


Fig. 12. (a) Spatial distribution of specific surface area in a sample of Berea sandstone deformed at  $P_{\text{eff}} = 90 \text{ MPa}$ . (b) Extensive grain crushing in a compaction zone. (c) Area in the periphery of the compaction zone where axial cracking dominate. (d) No damage outside the compaction zone. The  $\sigma_1$  direction is vertical.

Darley Dale sandstone (Fig. 15a) corresponds to the conventional conception of how failure mode evolves during the brittle–ductile transition (Bernabé and Brace, 1990; Mair et al., 2002), involving high-angle conjugate shear bands that may readily appear on the exterior surface of a failed sample. Since compaction band formation was inhibited in the Darley Dale sandstone that has the lowest porosity, our data suggest that compaction bands develop preferentially in more porous sandstones. To elucidate the development of compaction bands in the other sandstones it was necessary to conduct detailed AE and microstructural observations (DiGiovanni et al., 2000; Olsson and Hol-

comb, 2000; Wong et al., 2001). Our microstructural observations not only document the pervasive occurrence of compaction bands as a mode of localization, but also highlight the geometric complexity of such bands, which may propagate as discrete or diffuse entities.

#### 6.2. Bifurcation analysis, damage evolution and AE activity

The mechanics of compaction localization can be analyzed as a bifurcation in the constitutive response of a porous medium. Critical conditions for the inception of localization and orientations of the compactive shear and

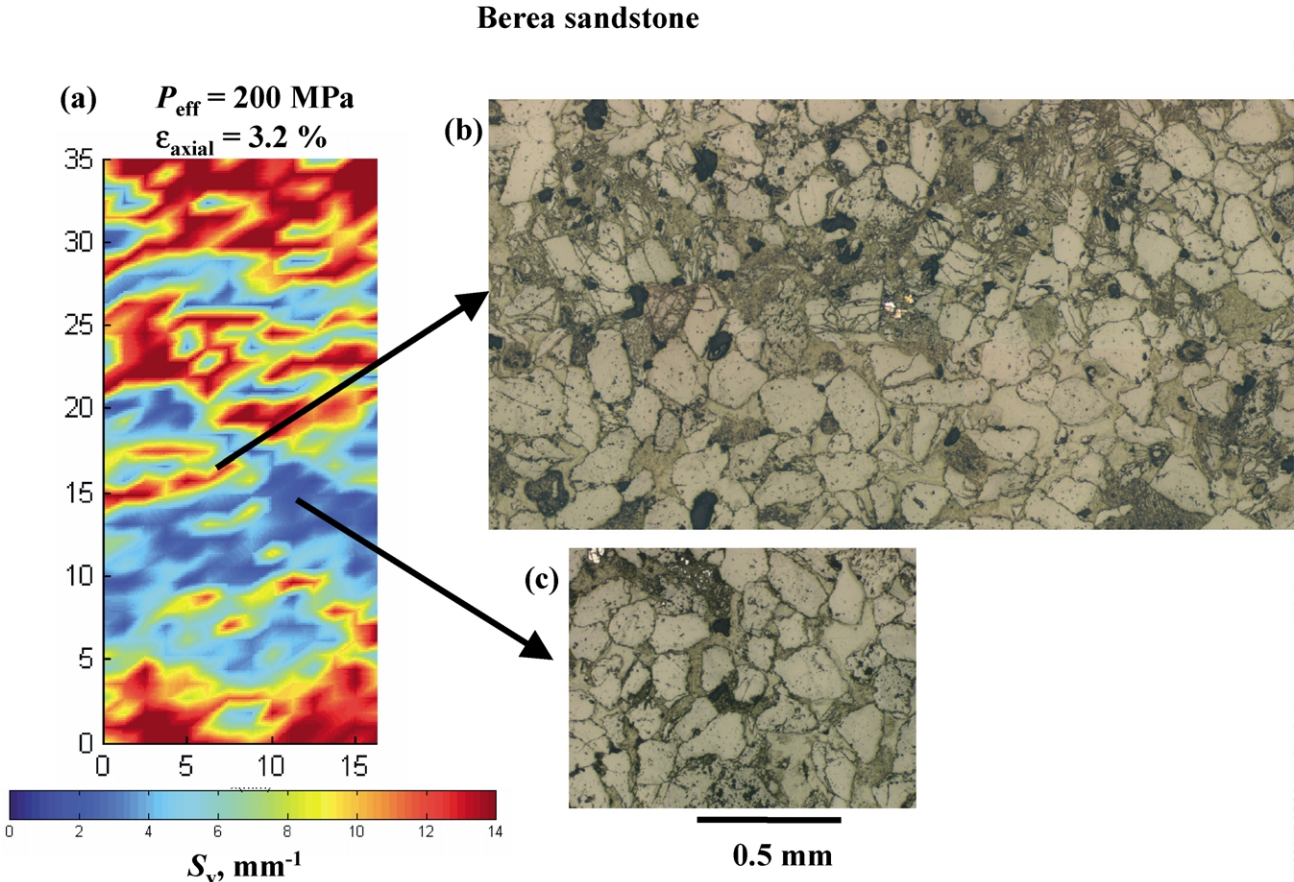


Fig. 13. (a) Spatial distribution of specific surface area in a sample of Berea sandstone deformed at  $P_{\text{eff}} = 200 \text{ MPa}$ . This sample presented diffused compaction zones as well as discrete compaction bands (b) mosaic of micrographs showing the transition between a discrete compaction band and an undamaged zone. (c) Some areas of the sample remained undamaged. The  $\sigma_1$  direction is vertical.

compaction bands can be derived as functions of the constitutive parameters. The simplest approach is to adopt a constitutive relation whereby the yield envelope and inelastic volumetric change can be characterized by the pressure-sensitivity parameter  $\mu$  and dilatancy factor  $\beta$ , respectively (Rudnicki and Rice, 1975; Olsson, 1999; Bésuelle, 2001). For this model with one yield surface, Isen and Rudnicki (2000) derived the general condition  $\beta + \mu \leq -\sqrt{3}$  for inception of compaction band under axisymmetric compression. Wong et al. (2001) observed that the mechanical data on sandstone samples that failed by compaction localization satisfy the conditions  $-\sqrt{3}/2 < \beta < 0$  and  $\mu > -\sqrt{3}/2$ , which disagree with the theoretical prediction for the constitutive model with one yield surface. They attributed the discrepancy to the inadequacy of this constitutive model, and argued that since failure in the transitional regime involves the partitioning of damage between at least two mechanism (axial microcracks that may grow and coalesce to form a shear fault, and pores that collapse while grains are crushed) it may be necessary to use a more elaborate model such as that formulated by Isen (2002) that incorporates two yield surfaces. Predictions of this recent model are in better agreement with the mechan-

ical data of Wong et al. (2001) for the Berea, Bentheim and Darley Dale sandstones.

While bifurcation analysis provides a very useful framework for understanding the mechanics of compaction localization, it has an intrinsic limitation that the analysis applies only to the onset of constitutive instability in an initially homogeneous material and does not provide any information on the subsequent propagation behavior or geometric attributes of the localization structures. In particular this continuum approach cannot explain why compaction bands may develop as discrete or diffuse structures.

An explanation may lie in the microstructure. Discrete compaction bands have primarily been observed in highly porous materials with relatively homogeneous and regular pore structures. In cellular solids such as honeycombs (e.g. Papka and Kyriakides, 1999) and metal foams (e.g. Bastawros et al., 2000) subparallel arrays of discrete compaction bands have been observed to develop while the stress-strain curves registered episodic stress drops. The I → II transformation in ice occurs at critical stress states (Durham et al., 1983) qualitatively similar to the compactive yield envelopes shown in Fig. 15. This transformation is associated with a significant volume reduction (of ~21%)

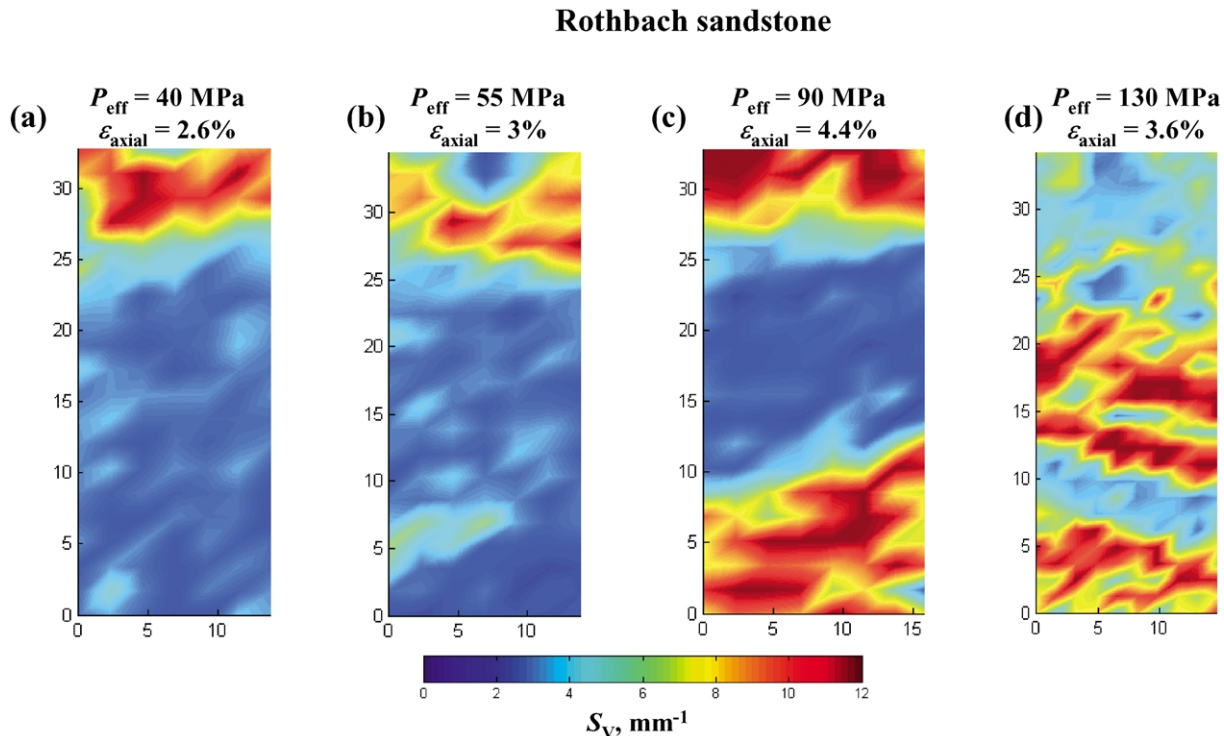


Fig. 14. Spatial distribution of specific surface area in samples of Rothbach sandstone deformed in the brittle-ductile transition at 40 MPa (a), 55 MPa (b), 90 MPa (c), and 130 MPa (d) effective pressure. The  $\sigma_1$  direction is vertical.

and it has been observed to involve discrete compaction bands (Kirby et al., 1992). In the present study arrays of discrete compaction bands were observed only in the two most porous sandstones.

However, porosity may not be the only microstructural attribute that promotes the development of discrete compaction bands. In the Castlegate sandstone Olsson and Holcomb's (2000) AE data indicate that the mode of compaction localization involves diffuse and not discrete bands, even though it has an initial porosity of 28%, which is higher than those of the five sandstones investigated in this study. Since rather limited stress conditions were considered in their study, it is unclear whether discrete compaction bands may actually develop in Castlegate sandstone under other pressure conditions associated with the brittle–ductile transition. Klein et al. (2001) speculated that discrete compaction band is predominant in the Bentheim sandstone possibly due to its relatively homogeneous mineralogy (with 95% quartz) and well-sorted grain sizes. However we document in this study that the mode of compaction localization in the Diemelstadt sandstone is very similar to the Bentheim sandstone, and since the former has a modal composition with 26% feldspar (Table 1), this implies that mineralogical homogeneity may not be necessary for the development of discrete compaction bands. Other than having similar porosities, both Bentheim and Diemelstadt sandstones have a relatively narrow grain size distribution (Klein, 2002). If the propagation of discrete bands over long distances are readily arrested in an

aggregate with relatively disperse grain sizes and small pores, this may provide a plausible explanation for the absence of arrays of discrete compaction bands in the other sandstones.

Our microstructural observations suggest that the compaction bands in Berea and Rothbach sandstones initiated as short discrete features that were arrested before propagating across the sample, and many such short discrete bands subsequently coalesced to develop a mosaic of diffuse bands. A conceptual model of how diffuse bands may develop from coalescence is illustrated in Fig. 16b. Since the experiments on the Bentheim sandstone presented here were for nominally dry samples, one may also speculate that the propagation of discrete bands may also be stabilized in the presence of water. However, we have performed parallel experiments on samples saturated with water and the failure mode and microstructure are qualitatively similar to what we present here for the dry samples. It should also be noted that a similar localization mode was observed in saturated samples of the Diemelstadt sandstone.

A deeper understanding of the micromechanics will help address some of these intriguing questions on compaction localization. It is useful in such an investigation to integrate AE and microstructural observations. We have demonstrated that categorization of AE activity into the  $p$ - and  $m$ -types provides a diagnostic tool for distinguishing the development and absence of compaction bands. In  $p$ -type AE activity the occurrence of multiple pulses strongly suggest that compaction bands nucleate as discrete features

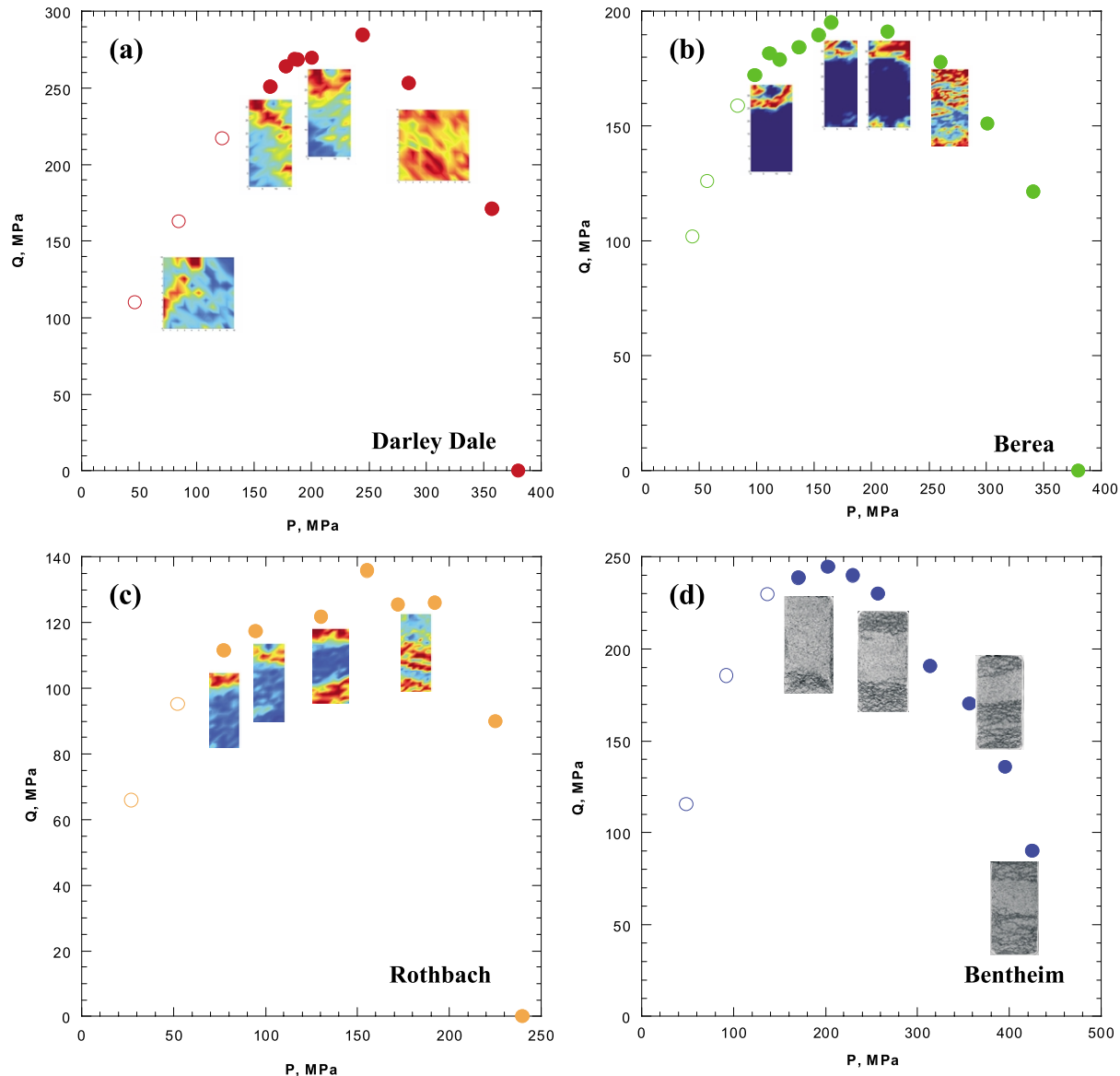


Fig. 15. Peak stresses and yield stresses at the onset of shear-enhanced compaction for Darley Dale (a), Berea (b), Rothbach (c) and Bentheim sandstones (d).

even though they may subsequently coalesce into a more diffuse structure. Even though our study used a single AE transducer, more extensive AE measurements using multiple AE transducers can provide detailed information on the AE locations and spatial clustering of damage. In particular, the evolution of diffuse compaction bands in the Castlegate sandstone (with 28% porosity) has been carefully mapped out by [Olsson and Holcomb \(2000\)](#).

The intensity of damage can be inferred from either the mechanical or stereological data. For the Bentheim sandstone the failed samples did not show appreciable barreling, with the implication that the porosity reduction was mainly due to axial shortening with negligible radial strains. Indeed if we plot the volumetric strain as a function of axial strain for samples deformed in the regime where compaction bands developed, they follow a linear trend with slope close to unity ([Fig. 17](#)). As an example we analyzed

the data for the experiment at 300 MPa confining pressure. From the mechanical and AE data ([Fig. 2b](#)) we estimate that an AE pulse typically occurred over an inelastic axial strain of  $\sim 0.2\%$  (corresponding to a shortening of  $\Delta\ell \sim 76 \mu\text{m}$  in a sample of nominal length 38.1 mm). Since our microstructural observations ([Fig. 9](#)) indicate that the damage due to one such pulse was sustained primarily in a single discrete compaction band with a lateral dimension of one to two grains ( $\ell \sim 500 \mu\text{m}$ ), we infer that the localized compaction inside the band would be  $\Delta\ell/\ell \sim 15\%$ . Since the Bentheim sandstone has an initial porosity of 23%, such inelastic deformation would necessitate significant pore collapse. Indeed the inelastic compaction and comminution in the discrete bands were so intense that we found it difficult to quantify the damage unless we resorted to microscopic observations under very high magnifications.

In the other sandstones we conducted stereological

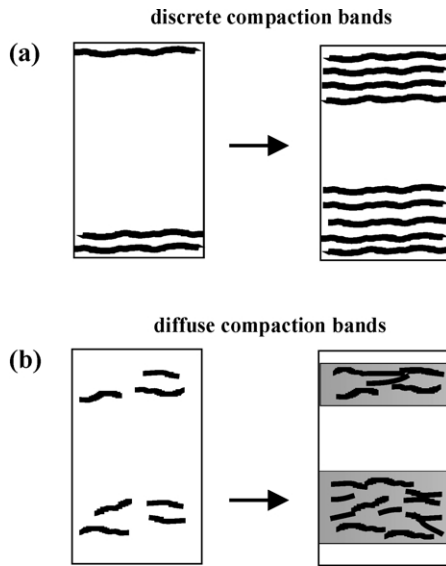


Fig. 16. Conceptual models for the initiation and development of (a) discrete and (b) diffuse compaction bands in porous sandstones.

measurements to map out the damage intensity. While the damage maps provide details on the spatial distribution, for comparative purposes it is also useful to evaluate the average values. However, because damage was distributed in a very heterogeneous way in most of our samples averaging over the entire sample would not provide useful information on the localized damage. Therefore in Table 3 we present for each deformed sample several average values of the stereological parameters computed for localized areas where  $S_v$  exceeded a certain threshold. The first threshold values correspond to the nominal damage in unstressed samples (Menéndez et al., 1996; Wu et al., 2000), and hence

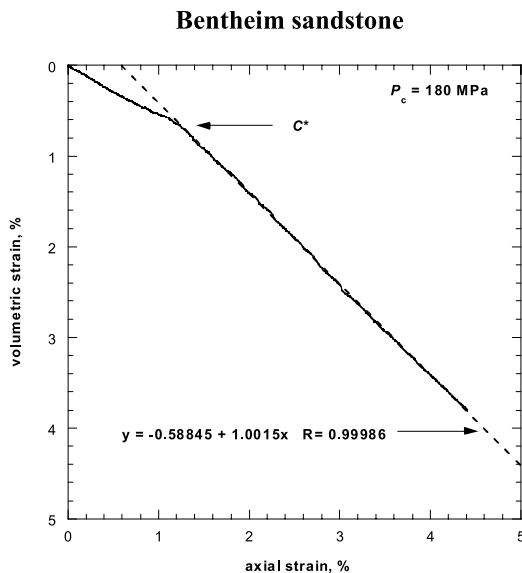


Fig. 17. Volumetric strain versus axial strain for a sample of Bentheim sandstone deformed at 180 MPa. After  $C^*$ , the slope of the curve is close to one.

the computed averages correspond to the stress-induced damage.

Our measurements for samples deformed in the transitional regime are in overall agreement with previous data of Menéndez et al. (1996) and Wu et al. (2000) for samples deformed in the brittle faulting and ductile flow regimes. An anisotropy factor  $\Omega_{23}$  on the order of 0.1 was observed in most of the sample, indicating that stress-induced anisotropy may play an important role in the development of compaction localization as suggested recently in Rudnicki's (2002) bifurcation analysis. It should also be noted that Eqs. (1) and (2) are valid only for an axisymmetric distribution of microcracks (Wong, 1985), and therefore the stereological parameters so derived may not truly represent the damage in samples that developed high-angle shear bands that cannot be approximated as axisymmetric deformation.

### 6.3. Comparison with field observations

Systematic studies in the rock mechanics laboratory have demonstrated that compaction localization is associated with stress states in the transitional regime from brittle faulting to cataclastic flow. The stress states are in the range typically encountered in sedimentary formations (Fig. 15). The laboratory results therefore suggest that localized structures such as compaction bands and high-angle shear bands can be pervasive in sandstone formations, not just limited to the aeolian Navajo sandstone in which they were first observed (Mollema and Antonellini, 1996). Indeed Sternlof and Pollard (2002) recently documented field evidence for the abundant development of compaction bands in the Jurassic Aztec sandstone of southeastern Nevada.

While a number of localized structures have been postulated to be subperpendicular to  $\sigma_1$ , it should be noted that the operative deformation mechanisms are distinctly different. In a mature strike-slip fault (such as the San Andreas system), fault normal compression is attributed to mechanical weakness in both absolute and relative senses (Rice, 1992; Hickman et al., 1995). Diffusive mass transfer (pressure solution) may also induce stylolites to develop as discrete surfaces oriented normal to  $\sigma_1$  (Fletcher and Pollard, 1981). Since they can act as barriers to fluid transport and influence the stress field and strain partitioning in accretionary prisms and sedimentary formations, an important question is to what extent and under what conditions these localized compactant structures would occur. Recognition of such structures in the field would elucidate the tectonic processes by which localization in sandstone formations (Aydin and Johnson, 1978) and accretionary prisms (Byrne et al., 1993) develop. In geotechnical problems on a smaller scale, it has also been proposed that borehole breakouts in highly porous sandstone may occur by the propagation of compaction bands (Olsson, 1999; Haimson, 2001; Klaetsch and Haimson, 2002).

Table 3  
Quantitative microstructural data of deformed samples

Effective pressure (MPa)	Crack density for linear intercepts perpendicular to $\sigma_1$ ( $P_L^\perp$ : mm $^{-1}$ )	Crack density for linear intercepts parallel to $\sigma_1$ ( $P_L^\parallel$ : mm $^{-1}$ )	Crack area per unit volume ( $S_v$ : mm $^{-1}$ )	Anisotropy factor ( $\Omega_{23}$ )
Berea sandstone				
50				
$S_v > 4$	5.53	4.83	10.76	0.1
$S_v > 6$	5.89	5.11	11.45	0.11
$S_v > 8$	6.29	5.47	12.22	0.1
60				
$S_v > 4$	5.23	4.71	10.24	0.06
$S_v > 6$	5.75	5.06	11.02	0.09
$S_v > 8$	6.25	5.52	12.18	0.09
75				
$S_v > 4$	5.19	4.35	10.02	0.13
$S_v > 6$	5.56	4.66	10.73	0.12
$S_v > 8$	6.44	5.35	12.41	0.14
90				
$S_v > 4$	4.58	4.05	8.93	0.086
$S_v > 6$	5.34	4.66	10.39	0.1
$S_v > 8$	5.87	5.12	11.42	0.1
150				
$S_v > 4$	5.34	5.15	10.06	0.03
$S_v > 6$	5.98	5.79	11.88	0.02
$S_v > 8$	6.29	6.11	12.5	0.02
200				
$S_v > 4$	4.4	4.19	8.7	0.006
$S_v > 6$	5.52	5.09	10.85	0.04
$S_v > 8$	6.38	5.81	12.52	0.064
$S_v > 8$	6.95	6.29	13.62	0.067
Darley Dale sandstone				
80				
	3.78	3.3	7.35	0.05
$S_v > 2$	3.78	3.31	7.35	0.05
$S_v > 4$	4.05	3.49	7.86	0.08
$S_v > 6$	4.87	3.95	9.34	0.14
$S_v > 8$	5.71	4.48	10.9	0.17
90				
	3.54	3.09	6.89	0.07
$S_v > 2$	3.54	3.09	6.89	0.07
$S_v > 4$	3.83	3.31	7.44	0.09
$S_v > 6$	4.73	3.94	9.12	0.12
$S_v > 8$	5.62	4.49	10.76	0.16
95				
	3.59	2.99	6.92	0.12
$S_v > 2$	3.71	3.08	7.16	0.12
$S_v > 4$	4.32	3.56	8.3	0.14
$S_v > 6$	4.96	4.04	9.53	0.15
$S_v > 8$	5.66	4.56	10.84	0.16
110				
	3.31	2.81	6.04	0.11
$S_v > 2$	3.36	2.84	6.5	0.11
$S_v > 4$	3.44	2.91	6.66	0.12
$S_v > 6$	3.85	3.19	7.42	0.14
$S_v > 8$	4.56	3.7	8.75	0.15
Rothbach sandstone				
40				
	2.03	1.9	4	0.008
$S_v > 2$	2.21	2.04	4.35	0.029
$S_v > 8$	5.29	4.58	10.28	0.104
55				
	1.96	1.87	3.88	-0.012
$S_v > 2$	2.31	2.16	4.56	0.035
$S_v > 8$	4.92	4.61	9.69	0.04
90				
	3.17	2.87	6.21	0
$S_v > 2$	3.8	3.39	7.43	0.045
$S_v > 8$	5.74	4.86	11.1	0.12
130				
	3.58	3.38	7.07	0.027
$S_v > 2$	3.58	3.38	7.07	0.027
$S_v > 10$	6.11	5.52	11.97	0.08

The field observations (Mollema and Antonellini, 1996; Sternlof and Pollard, 2002) point to subparallel arrays of relatively narrow compaction bands akin to what are characterized as discrete compaction bands in the present study. However, the laboratory studies have also documented the alternative development of compaction bands as diffuse structures. A question therefore arises as to whether diffuse compaction bands also develop in the field, and if so, why they have not been observed.

While this is a question that can only be addressed by more systematic investigations in the field, we have begun to identify the key microstructural attributes that are favorable for the development of compaction localization in the form of discrete bands, such as those in the Bentheim and Diemelstadt sandstones, as well as in cellular solids and ice. One should also keep in mind that even in laboratory-deformed sandstones, the complex mosaic of diffuse compaction bands could not be delineated without comprehensive and tedious measurements, especially in the highly deformed samples with diffuse bands covering a relatively large proportion of the sample. As discussed above, we had to conduct stereological measurements at relatively fine scale to map out the spatial heterogeneity of damage in the Berea and Rothbach sandstones. Similarly, the diffuse compaction bands in the Castlegate sandstone could not have been resolved by Olsson and Holcomb (2000) without their high-resolution AE measurement system.

While the laboratory studies have provided a very useful analog for understanding the mechanics of compaction localization in the field, there are several apparent discrepancies. Grain crushing as a mechanism of pore collapse seems to be not as pronounced in the field examples as the discrete compaction bands in our Bentheim and Diemelstadt sandstone samples. In many instances the compaction bands in the field have propagated transverse to the bedding (K. Sternlof, personal communication, 2002), whereas the samples in this study were all cored perpendicular to bedding and therefore the compaction bands had all propagated parallel to the bedding. These outstanding questions should be addressed by a more systematic integration of mechanical data, structural observations and theoretical analyses in future studies.

Most laboratory studies on initially intact samples show that compaction localization tends to initiate and cluster near either end of a sample, with the implication that the bands have possibly been triggered by the local stress heterogeneity due to the end-constraints. In geologic settings structural and stress heterogeneities are pervasive on all scales, and a deeper understanding of how they control the initiation of compaction localization necessitates studying the process under well-defined conditions of stress concentration. To address this question Vajdova and Wong (2003) recently conducted triaxial compression tests on circumferentially notched samples of Bentheim sandstone, and their data illustrate how compaction bands can

initiate from the notch tips and propagate by sequential increments as ‘anti-cracks’ in a manner analogous to field observations.

## 7. Conclusion

Integrating mechanical deformation, AE and microstructural observations, we have demonstrated that localized failure modes involving compaction bands and high-angle shear bands can develop in five sandstones with porosities ranging from 13 to 24% while they undergo shear-enhanced compaction. We also confirm that such phenomena of compaction localization are commonly associated with stress states in the transitional regime from brittle faulting to cataclastic flow. Our observations have documented a broad spectrum of geometric complexity associated with compaction localization, and we identify two end-members of localization mode: shear bands at relatively high angles and arrays of discrete compaction bands subperpendicular to the maximum compression direction, which have been observed in the most compact (Darley Dale) and porous (Bentheim and Diemelstadt) sandstones, respectively. In (Berea and Rothbach) sandstones with intermediate porosities we also observed a hybrid localization mode involving high-angle shear bands and diffuse compaction bands.

The various localization modes are manifested by distinct AE signatures. Whereas the development of high-angle shear bands is characterized by the continuous accumulation of AE (*m*-type activity), discrete bands are associated with episodic surges in AE (*p*-type activity) that are characterized by an overall strain hardening trend punctuated by episodic stress drops. The number of discrete bands correlates with the number of AE surges and stress drops.

The discrete compaction bands in our sandstone samples are akin to those documented in cellular solids and metal foams with highly porous and relatively homogeneous structures. A similar localization mode has been observed in ice during the high-pressure I → II transformation that involves 21% volume reduction. In relation to tectonic deformation, arrays of discrete compaction bands with qualitatively similar features have also been documented in Navajo and Aztec sandstone formations.

## Acknowledgements

We thank Veronika Vajdova for her precious help in the laboratory, Michel Darot for helping to collect extra Bentheim sandstone, and Jérôme Fortin for helping with the experiments on Diemelstadt sandstone. Kurt Sternlof and Dave Pollard have graciously shared with us their field observations. We thank Pierre Bésuelle, Joanne Fredrich, Yves Guégan, Bezalel Haimson, Dave Holcomb, Steve Kirby, Bill Olsson and John Rudnicki for stimulating

discussions regarding compaction localization. Patrick Baud was partially supported by Université Louis Pasteur. The research at Stony Brook was partially supported by the National Science Foundation under grants EAR-0106580 (in collaboration with Kathleen Issen of Clarkson University) and INT-9815570 (in collaboration with Yves Guéguen of Ecole Normale Supérieure, Paris).

## References

- Aydin, A., Johnson, A.M., 1978. Development of faults as zones of deformation bands and as slip surfaces in sandstone. *Pure and Applied Geophysics* 116, 931–942.
- Bastawros, A.-F., Bart-Smith, H., Evans, A.G., 2000. Experimental analysis of deformation mechanisms in a closed-cell aluminum alloy foam. *Journal of the Mechanics and Physics of Solids* 48, 301–322.
- Baud, P., Zhu, W., Wong, T.-f., 2000. Failure mode and weakening effect of water on sandstone. *Journal of Geophysical Research* 105, 16371–16389.
- Bernabé, Y., Brace, W.F., 1990. Deformation and fracture of Berea sandstone. In: Duba, A.G., Durham, W.B., Handin, J.W., Wang, H.F. (Eds.), *The Brittle–Ductile Transition in Rocks*. American Geophysical Union Monograph 56, pp. 91–101.
- Bésuelle, P., 2001. Compacting and dilating shear bands in porous rocks: theoretical and experimental conditions. *Journal of Geophysical Research* 106, 13435–13442.
- Bésuelle, P., Desrues, J., Raynaud, S., 2000. Experimental characterization of the localization phenomenon inside a Vosges sandstone in a triaxial cell. *International Journal of Rock Mechanics and Mining Sciences* 37, 1223–1237.
- Bésuelle, P., Baud, P., Wong, T.-f., 2003. Failure mode and spatial distribution of damage in Rothbach sandstone in the brittle-ductile transition. *Pure and Applied Geophysics* 160, 851–868.
- Byrne, T., Maltman, A., Stephenson, E., Soh, W., Knipe, R., 1993. Deformation structures and fluid flow in the toe region of the Nankai accretionary prism. *Proceedings of the ODP, Scientific Results* 131, 83–192.
- DiGiovanni, A.A., Fredrich, J.T., Holcomb, D.J., Olsson, W.A., 2000. Micromechanics of compaction in an analogue reservoir sandstone. *Proceedings of the 4th North American Rock Mechanics Symposium*, pp. 1153–1160.
- Durham, W.B., Heard, H.C., Kirby, S.H., 1983. Experimental deformation of polycrystalline H<sub>2</sub>O ice at high pressure and low temperature: preliminary results. *Journal of Geophysical Research* 88, B377–B392.
- El Bied, A., Sulem, J., Martineau, F., 2002. Microstructure of shear zones in Fontainebleau sandstone. *International Journal of Rock Mechanics and Mining Sciences* 39, 917–932.
- Fletcher, R.C., Pollard, D.D., 1981. Anticrack model for pressure solution surfaces. *Geology* 9, 419–424.
- Fortin, J., Baud, P., Wong, T.-f., 2003. Mechanical Compaction of Diemelstadt Sandstone: From Compacting Shear Bands to Compaction Bands (abstract). EGS-AGU Meeting, Nice.
- Haimson, B.C., 2001. Fracture-like borehole breakouts in high porosity sandstone: are they caused by compaction bands? *Physics and Chemistry of the Earth (A)* 26, 15–20.
- Handin, A., Hager, R.V., Friedman, M., Feather, J.N., 1963. Experimental deformation of sedimentary rock under confining pressure: pore pressure effects. *Bulletin of the American Association of Petroleum Geologists* 47, 717–755.
- Hickman, S., Sibson, R., Bruhn, R., 1995. Introduction to special issue: mechanical involvement of fluids in faulting. *Journal of Geophysical Research* 100, 12831–12840.
- Issen, K.A., 2002. The influence of constitutive models on localization conditions for porous rock. *Engineering Fracture Mechanics* 69, 1891–1906.
- Issen, K.A., Rudnicki, J.W., 2000. Conditions for compaction bands in porous rock. *Journal of Geophysics Research* 105, 21529–21536.
- Kirby, S.H., Durham, W.B., Stern, L., 1992. The ice I → II transformation: mechanisms and kinetics under hydrostatic and nonhydrostatic conditions. In: Maeno, N., Hondoh, T. (Eds.), *Physics and Chemistry of Ice*. Hokkaido University Press, Sapporo, pp. 456–463.
- Klaetsch, A.R., Haimson, B., 2002. Porosity-dependent fracture-like breakouts in St. Peter sandstone. In: Hammah et al. (Eds.), NARMS-TAC 2002, University of Toronto, ISBN: 0-7727-6708-4, vol. 2, pp. 1365–1371.
- Klein, E., 2002. *Micromécanique des Roches Granulaires Poreuses: Expérimentation et Modélisation*. Thèse de doctorat, Université Louis Pasteur, Strasbourg, France.
- Klein, E., Baud, P., Reuschlé, T., Wong, T.-f., 2001. Mechanical behavior and failure mode of Bentheim sandstone under triaxial compression. *Physics and Chemistry of the Earth (A)* 26, 21–25.
- Mair, K., Main, I., Elphick, S., 2000. Sequential growth of deformation bands in the laboratory. *Journal of Structural Geology* 22, 25–42.
- Mair, K., Elphick, S.C., Main, I.G., 2002. Influence of confining pressure on the mechanical and structural evolution of laboratory deformation band. *Geophysical Research Letters* 29(10) (DOI: 10.1029/2001L013964).
- Menéndez, B., Zhu, W., Wong, T.-f., 1996. Micromechanics of brittle faulting and cataclastic flow in Berea sandstone. *Journal of Structural Geology* 18, 1–16.
- Mollema, P.N., Antonellini, M.A., 1996. Compaction bands: a structural analog for anti-mode I cracks in aeolian sandstone. *Tectonophysics* 267, 209–228.
- Olsson, W.A., 1999. Theoretical and experimental investigation of compaction bands in porous rock. *Journal of Geophysical Research* 104, 7219–7228.
- Olsson, W.A., Holcomb, D.J., 2000. Compaction localization in porous rock. *Geophysical Research Letters* 27, 3537–3540.
- Papka, S.D., Kyriakides, S., 1999. Biaxial crushing of honeycombs—Part I: experiments. *International Journal of Solids and Structures* 36, 4367–4396.
- Rice, J.R., 1992. Fault stress states, pore pressure distributions, and the weakness of the San Andreas fault. In: Evans, B., Wong, T.-f. (Eds.), *Fault Mechanics and Transport Properties of Rocks*, Academic Press, San Diego, pp. 475–504.
- Rudnicki, J.W., 2002. Conditions for compaction and shear bands in a transversely isotropic material. *International Journal of Solids and Structures* 39, 3741–3756.
- Rudnicki, J.W., Rice, J.R., 1975. Conditions for the localization of deformation in pressure sensitive dilatant materials. *Journal of the Mechanics and Physics of Solids* 23, 371–394.
- Schock, R.N., Heard, H.C., Stephens, D.R., 1973. Stress-strain behavior of a granodiorite and two graywackes on compression to 20 Kilobars. *Journal of Geophysical Research* 78, 5922–5941.
- Sternlof, K., Pollard, D.D., 2002. Numerical modeling of compactive deformation bands as granular “anti-cracks”. *Eos Translations AGU* 83 (47), T11F-10.
- Underwood, E.E., 1970. *Quantitative Stereology*. Addison Wesley, Reading, 274pp.
- Vajdova, V., Wong, T.-f., 2003. Incremental propagation of discrete compaction bands: acoustic emission and microstructural observations on circumferentially notched samples of Bentheim sandstone. *Geophysical Research Letters* 30 (14), 1775 DOI: 10.1029/2003GL017750.
- Wong, T.-f., 1985. Geometric probability approach to the characterization and analysis of microcracking in rocks. *Mechanics of Materials* 4, 261–276.
- Wong, T.-f., David, C., Zhu, W., 1997. The transition from brittle faulting to cataclastic flow in porous sandstones: mechanical deformation. *Journal of Geophysical Research* 102, 3009–3025.
- Wong, T.-f., Baud, P., Klein, E., 2001. Localized failure modes in a compactant porous rock. *Geophysical Research Letters* 28, 2521–2524.

- Wu, X.Y., Baud, P., Wong, T.-f., 2000. Micromechanics of compressive failure and spatial evolution of anisotropic damage in Darley Dale sandstone. International Journal of Rock Mechanics and Mining Sciences 37, 143–160.
- Zhang, J., Wong, T.-f., Davis, M.D., 1990. High pressure embrittlement and shear-enhanced compaction in Berea sandstone: acoustic emission measurement and microstructural observation. In: Hustrulid, W.A., Johnson, G.A. (Eds.), Rock Mechanics Contributions and Challenges, Proceedings of 31st U.S. Symposium on Rock Mechanics, pp. 653–660.